### nature physics

**Article** 

https://doi.org/10.1038/s41567-023-02223-z

# Laser ablation and fluid flows reveal the mechanism behind spindle and centrosome positioning

Received: 3 February 2022

Accepted: 23 August 2023

Published online: 2 November 2023



Check for updates

Hai-Yin Wu 12, Gökberk Kabacaoğlu, Ehssan Nazockdast, A Huan-Cheng Chang<sup>5</sup>, Michael J. Shelley © <sup>3,6</sup> & Daniel J. Needleman<sup>2,3,7</sup>

Few techniques are available for studying the nature of forces that drive subcellular dynamics. Here we develop two complementary ones. The first is femtosecond stereotactic laser ablation, which rapidly creates complex cuts of subcellular structures and enables precise dissection of when, where and in what direction forces are generated. The second is an assessment of subcellular fluid flows by comparison of direct flow measurements using microinjected fluorescent nanodiamonds with large-scale fluid-structure simulations of different force transduction models. We apply these techniques to study spindle and centrosome positioning in early Caenorhabditis elegans embryos and to probe the contributions of microtubule pushing, cytoplasmic pulling and cortical pulling upon centrosomal microtubules. Based on our results, we construct a biophysical model to explain the dynamics of centrosomes. We demonstrate that cortical pulling forces provide a general explanation for many behaviours mediated by centrosomes, including pronuclear migration and centration, rotation, metaphase spindle positioning, asymmetric spindle elongation and spindle oscillations. This work establishes methodologies for disentangling the forces responsible for cell biological phenomena.

The movement and positioning of centrosomes, microtubule (MT) organizing centres, govern many important phenomena in cell biology, including the orientation and positioning of the spindle<sup>1-8</sup>, the position of the nucleus 9-11 and the migration of pronuclei 12,13. Centrosomes display three basic behaviours in various systems: (1) directed motion<sup>7,12–15</sup>, (2) stable positioning<sup>7,16,17</sup> and (3) oscillations<sup>18–20</sup>. All of these behaviours are observed in early Caenorhabditis elegans embryos. The pronuclear complex (PNC) undergoes directed motion to the cell centre with its two centrosomes becoming aligned with the embryo's long axis14. The spindle then forms between the two centrosomes and is stably positioned in the cell centre<sup>16</sup>. Finally, as the spindle elongates and is positioned asymmetrically, it and its centrosomes undergo transverse oscillations 14,19,21-24. It is poorly understood how these different behaviours arise from the underlying mechanical and biochemical processes, although extensive work demonstrates the importance of astral MTs<sup>25-29</sup> that radiate outward from the centrosomes and of the molecular motor dynein<sup>30-37</sup>.

All movements in cells result from forces. Due to the small size of the centrosomes (<10  $\mu$ m), their slow speeds (<1  $\mu$ m s<sup>-1</sup>) and the viscous nature of the cytoplasm (>100 mPa s), the Reynolds number associated

Department of Physics, Harvard University, Cambridge, MA, USA. Department of Molecular and Cellular Biology, Harvard University, Cambridge, MA, USA. 3 Center for Computational Biology, Flatiron Institute, Simons Foundation, New York, NY, USA. 4 Department of Applied Physical Sciences, University of North Carolina, Chapel Hill, NC, USA. 5 Institute of Atomic and Molecular Sciences, Academia Sinica, Taipei, Taiwan. 6 Courant Institute of Mathematical Sciences, New York University, New York, NY, USA. 7 John A. Paulson School of Engineering and Applied Sciences, Harvard University, Cambridge, MA, USA. e-mail: hywu@g.harvard.edu

with their motion is Re  $< 10^{-7} \ll 1$ . Thus, inertial forces are negligible in comparison to viscous forces. Consequently, the velocity of a centrosome is proportional to the forces acting upon it. Thus, a central challenge is to identify the origin of those forces yielding these distinct behaviours of centrosomes (that is directed motions, stable positioning and oscillations). Most proposals centre around three possible types of forces acting through astral MTs: MTs pushing on the cortex, MTs pulled by force generators anchored to the cortex and MTs pulled by force generators in the cytoplasm  $^{38}$ .

Here, we develop biophysical approaches to unambiguously determine the extent to which different centrosome motions in one-cell Caenorhabditis elegans embryos are driven by MT pushing or pulling, and if pulling, whether it is of cortical or cytoplasmic origin. This relies on several advances. First, we developed and utilized femtosecond stereotactic laser ablation (FESLA) as a versatile tool for dissecting when, where and in what direction forces originate. From our ablation studies, we conclude that pulling forces dominate during PNC migration and rotation, spindle centring, elongation and oscillations. Second, at all these stages, we compared subcellular flow measurements using microinjected fluorescent nanodiamonds (FNDs) with large-scale fluid dynamics simulations of flows resulting from pulling forces on astral MTs, from either force generators residing on the cortex or in the cytoplasm. The simulations of the former showed remarkable agreement with flow measurements, whereas those of the latter were profoundly different. This supports the hypothesis of pulling originating from the cortex, while also demonstrating that subcellular flows can encode in their structure a powerful signature of the mechanical basis of force generation. Finally, we constructed a coarse-grained theory, amenable to analysis, for centrosome motion that directly relates the biophysical properties of MT nucleation, growth and interaction with cortical force generators to the cell biological behaviour of centrosomes. This theory demonstrates that cortical pulling alone is sufficient to explain centrosome behaviours. Taken together, our results argue that cortical pulling forces provide a unifying explanation of the diverse centrosome motions—directed, stable positioning and oscillations—found in C. elegans embryos. Given the ubiquity of these centrosome behaviours across cell biology and the proposed role of cortical pulling forces in many different contexts, the investigative framework presented here should be widely applicable.

#### Pulling forces drive spindle oscillations

We began by studying the transverse oscillations of the first mitotic spindle in the late metaphase to the anaphase in C. elegans embryos (Fig. 1a and Extended Data Fig. 1a). We used spinning-disc confocal microscopy to image GFP:: $\beta$ -tubulin and mCherry:: $\gamma$ -tubulin, and tracked the motion of the spindle poles using automated image analysis (Methods and Extended Data Fig. 1b–g). As others have noted, the anterior pole (Fig. 1a,b, orange) and the posterior pole (Fig. 1a,b, blue) oscillate out of phase with each other (Supplementary Video 1), with the posterior pole displaying larger amplitudes and more robust oscillations  $^{21,22}$ .

To investigate how astral MTs contribute to these motions, we utilized a new FESLA system capable of cutting three-dimensional (3D) patterns with highly controlled timing and location (Fig. 1c and Methods)<sup>39,40</sup>. FESLA utilizes a reduced-repetition-rate ultrafast femtosecond laser to produce highly localized cuts with submicrometre precision<sup>41–45</sup>. We sought to determine the relative contribution of the pushing and pulling forces to spindle oscillations by selectively cutting different populations of astral MTs. If a centrosome is being pushed from the rear, then cutting the astral MTs behind the centrosome will cause the oscillations to stop (Fig. 1d, left). Similarly, if a centrosome is being pulled forward, then cutting astral MTs in the front will halt its motion (Fig. 1d, right). We first used this approach to explore the forces acting on centrosomes when they are at the midpoint of their oscillation, moving with maximum speed (Fig. 1b, inset,  $T_{\rm m}$ ). When astral MTs in front of these centrosomes were cut, the centrosomes

immediately stopped moving along their original course (Fig. 1e, Supplementary Video 2 and Extended Data Fig. 2d), indicating that this forward movement was primarily driven by pulling from these astral MTs. The centrosomes subsequently moved in the opposite direction, suggesting that pulling forces are also exerted by the astral MTs at the rear of the centrosome. Cutting astral MTs at the rear of the centrosome during this same point in the oscillations only marginally impacted their velocity (Fig. 1f, Supplementary Video 2 and Extended Data Fig. 2d), suggesting that the downward pulling forces greatly dominate over upward pulling forces (Fig. 1g).

We next investigated the forces at the peak of the oscillation, when their velocity is zero (Fig. 1b, inset,  $T_p$ ). Cutting the astral MTs below the centrosome that faced the distant cortex inhibited the downward motion that occurs subsequent to this time in control embryos (Fig. 1h. Supplementary Video 2 and Extended Data Fig. 2d), indicating that the downward movement in control embryos is primarily driven by pulling from these astral MTs. The centrosomes subsequently moved in the opposite direction, suggesting that pulling forces are also exerted by the astral MTs above the centrosome. Cutting the astral MTs above the centrosome during this same point in the oscillation did not significantly impact the centrosomes subsequent returning motion (Fig. 1i, Supplementary Video 2 and Extended Data Fig. 2d). Taken together, these results indicate that, at the peaks of the oscillations, astral MTs exert net pulling forces on centrosomes. Since the centrosome has zero velocity at this point, the pulling forces from above and below the centrosome must be equal and opposite (Fig. 1j).

We next made cuts in the shape of an open cylinder around the posterior centrosome with the cylinder axis aligned with the transverse (y) axis (Fig. 2a), thereby severing the MTs perpendicular to the direction of oscillation (Fig. 2b,c, and Supplementary Video 3). The centrosomes continued to oscillate after cutting (Fig. 2d), with significant increases in amplitude immediately afterward (Fig. 2e and Extended Data Fig. 2g,h). We also observed oscillations after double (y-z) plane cuts made in the MTs in two planes orthogonal to the spindle axis, which left the perpendicular MTs of the remaining two planes intact (Extended Data Fig. 2e,h). Since the centrosomes still reversed direction after these cuts, this result demonstrates that the bending of MTs perpendicular to the oscillation axis<sup>46</sup> is not required for the restoring mechanism of the oscillations. It is possible that substantial pulling and pushing forces can simultaneously be exerted by different astral MTs located on the same side of the centrosome. To test this, we made cup-shape cuts to temporarily eliminate all MTs around centrosomes except for those extending to one transverse side (Fig. 2f,g). We observed that the centrosome rapidly moved very close to the cortex (Fig. 2h and Supplementary Video 3) after a cup cut, approaching a minimum distance of  $5.3 \pm 0.3 \,\mu m$  from the cortex, compared to  $9.7 \pm 0.2 \,\mu m$  in uncut embryos (Fig. 2i). Thus, pulling forces dominate over pushing forces from astral MTs on the same side of a centrosome. Furthermore, the observation that centrosomes approach very close to the cortices after cup cuts suggests that pushing forces do not substantially contribute to the restoring force during normal oscillations.

#### Cortical pulling forces drive spindle oscillations

We next investigated whether the pulling forces that act on centrosomes during transverse oscillations result from force generators in the cytoplasm (such as from dynein transporting organelles along MTs $^{47-50}$ ) or on the cell cortex  $^{2,14,30,35,37,51-56}$  (such as cortically anchored dynein or MT depolymerizers). Subcellular fluid flows provide a means to distinguish between these possibilities because cytoplasmically based pulling forces tend to produce flows in the direction opposite to MT motions, whereas cortically based pulling forces tend to produce flows in the same direction as MT motions (Fig. 3a).

We first simulated the effect of cytoplasmic forces generated by dynein transporting cargo along MTs at time  $T_{\rm m}$  (Fig. 1b, inset), which produced complex, 3D flows, consisting of multiple vortices (Fig. 3b,

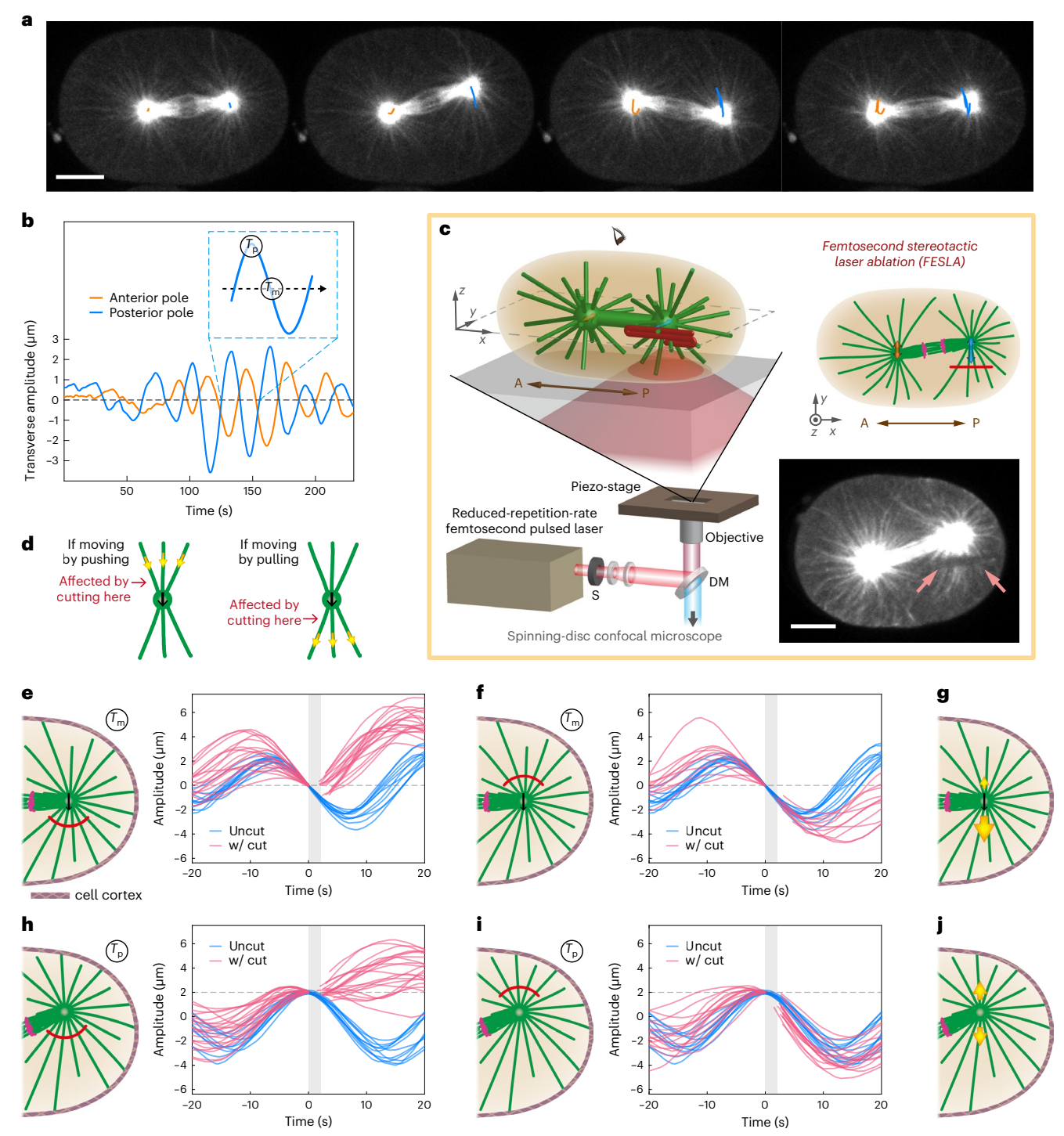


**Fig. 1**|Laser ablation during spindle oscillations in the first mitotic division of *C. elegans*. a, b, Spindle oscillations in a one-cell *C. elegans* embryo labelled with GFP::β-tubulin. a, One oscillation cycle and the corresponding trajectories of the anterior (orange) and posterior (blue) centrosomes (scale bar,  $10 \mu m$ ). b, Transverse amplitudes of the centrosomes and the definition of times  $T_p$  and  $T_m$ . c, FESLA. Left, the foci of a Ti:sapphire femtosecond pulsed laser with a reduced repetition rate (16-80 kHz) were scanned over the sample in a complex 3D pattern (red line) for ablation using a three-axis piezo-stage (MTs are in green; long brown arrow, the A–P axis; A, anterior; P, posterior; S, shutter; DM, dichroic mirror). Right, upper, 2D view of the x-y imaging plane (magenta, chromosomes; orange arrow, motion of the anterior centrosome; blue arrow, motion of the posterior centrosome). Right, lower, image of a sample after ablation. Arrows indicate the cut region (scale bar,  $10 \mu m$ ). d, Illustration of how cutting at different locations can distinguish between pushing and pulling scenarios. e-i, Arc-shaped cuts made in astral MTs on either transverse side of the posterior

centrosomes at two different time points in the oscillation cycle. At time  $T_{\rm m}({\bf e}-{\bf g})$ , the arc cuts in front of the centrosomes ( ${\bf e}$ ) and at the rear of the centrosomes ( ${\bf f}$ ) give the proposed net forces (yellow arrows) ( ${\bf g}$ ). At time  $T_{\rm p}$  ( ${\bf h}-{\bf j}$ ), the arc cuts below the centrosomes ( ${\bf h}$ ) and above the centrosomes ( ${\bf i}$ ) give the proposed net forces ( ${\bf j}$ ). See Extended Data Fig. 2b,c for the quantification:  $\Delta v_y = v_{\rm y(afrer)} - v_{\rm y(before)}$ . All statistical results are displayed in Extended Data Fig. 2d and presented as mean  $\pm$  standard error of the mean (SEM) as follows. At time  $T_{\rm m}$  ( ${\bf e},{\bf f}$ ),  $\Delta v_y = 0.05 \pm 0.05$  µm s<sup>-1</sup> in 11 uncut embryos (control).  ${\bf e}$ ,  $\Delta v_y = 0.86 \pm 0.06$  µm s<sup>-1</sup> in 18 arc-cut embryos with  $P = 5.0 \times 10^{-10}$ .  ${\bf f}$ ,  $\Delta v_y = -0.06 \pm 0.04$  µm s<sup>-1</sup> in 11 uncut embryos (control).  ${\bf h}$ ,  $\Delta v_y = 0.18 \pm 0.05$  µm s<sup>-1</sup> in 21 arc-cut embryos with  $P = 5.8 \times 10^{-10}$ .  ${\bf i}$ ,  $\Delta v_y = -0.61 \pm 0.04$  µm s<sup>-1</sup> in 16 arc-cut embryos with P = 0.28. The P values were calculated by two-tailed Student's t-tests based on the corresponding uncut and arc-cut data sets. See Extended Data Fig. 2a for the FESLA dimensions, w/cut, with cut.

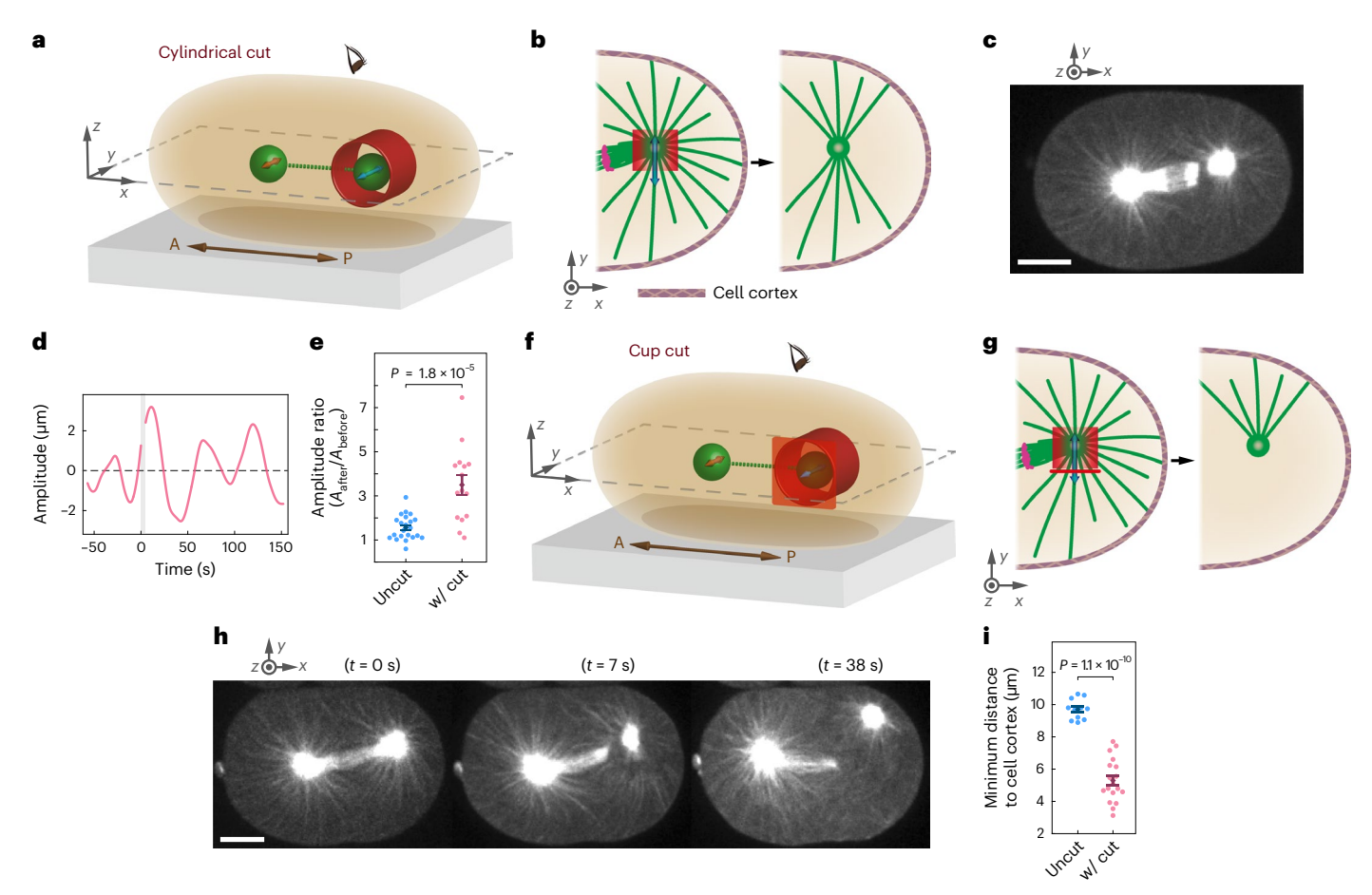


Fig. 2 | Open-cylindrical and cup cuts around the posterior centrosomes during spindle oscillations. Spindle poles are illustrated by green balls connected with green dashed lines in the 3D schematics  ${\bf a}$  and  ${\bf f}$ . The posterior portions of the x-y midplanes (view from the top) are shown in the corresponding 2D schematics  ${\bf b}$  and  ${\bf g}$ , with spindles and astral MTs in green and chromosomes in magenta. The ablation geometry is portrayed in red in all schematics.  ${\bf a}-{\bf e}$ , Opencylindrical cuts.  ${\bf a}$ , 3D schematic of a cut aligned along the transverse oscillation (y) axis.  ${\bf b}$ , 2D schematic showing the ablation of the MTs perpendicular to the oscillations, which leaves the transverse astral MTs intact.  ${\bf c}$ , An image taken directly after an open-cylindrical cut (scale bar, 10 µm).  ${\bf d}$ , Example of oscillation amplitudes before and after the cut, with the time of ablation marked by the light grey vertical strip.  ${\bf e}$ , The amplitudes of the oscillations increased after

open-cylindrical cuts were made. See Extended Data Fig. 2g for the quantification of the amplitude ratio.  $A_{\rm after}/A_{\rm before}=1.6\pm0.1$  in 22 uncut cycles, and  $A_{\rm after}/A_{\rm before}=3.5\pm0.4$  in 15 embryos with open-cylindrical cuts. **f-i**, Cup cuts. **f**, 3D schematic of a cut with opening facing in the transverse direction. **g**, 2D schematic showing the ablation of all astral MTs except those extending out from the opening of the cup. **h**, Images before and after a cup cut (scale bar,  $10~\mu m$ ). **i**, Comparison of the minimum distances from the approaching posterior centrosomes to the cell cortices, between uncut  $(9.7\pm0.2~\mu m, n=11)$  and cupcut  $(5.3\pm0.3~\mu m, n=18)$  embryos. See Extended Data Fig. 2j for the distance measurement. See Extended Data Fig. 2f, if or the FESLA dimensions. All data are presented as mean  $\pm$  SEM, and the P values were calculated using two-tailed Student's t-tests (error bars, SEM).

top). To help visualize these flows, we projected and averaged the flows in the two-dimensional (2D) plane of spindle motion (Fig. 3b, bottom). This flow pattern occurs because cytoplasmic pulling forces tend to create minus-end directed flows along MTs, but fluid incompressibility prevents these flows from being uniformly directed inward towards centrosomes. A very different pattern of flow is produced by simulating cortical pulling forces, as seen in both 3D (Fig. 3c, top) and 2D projections (Fig. 3c, bottom). In this case, the downward motion of the posterior centrosome leads to an overall rotational flow, with a much smaller, counterrotating backflow between the posterior centrosome and the cortex (Fig. 3c, bottom inset).

With these predictions in hand, we next experimentally measured cytoplasmic fluid flows in *C. elegans* embryos during spindle oscillations. We microinjected passivated  $^{57,58}$  FNDs  $^{59-64}$  into *C. elegans* syncytial gonads, which subsequently became incorporated into embryos (Methods). We imaged the FNDs and the spindle, labelled with green fluorescent protein (GFP)::\(\beta\)-tubulin, with 3D time-lapse spinning-disc confocal microscopy (Fig. 3d and Supplementary Video 4). We tracked the FNDs in 3D using automated image analysis

(Fig. 3d, right) and averaged the 2D projection of the FND trajectories from multiple embryos and multiple oscillations (Extended Data Fig. 3a,b and Methods). Figure 3e shows the resulting measured fluid flow throughout the embryo when the centrosomes are at the midpoint of their oscillations  $(T_m)$ . The measured fluid flow remarkably resembles that calculated from the cortical pulling model (compare Fig. 3c with Fig. 3e), displaying both the characteristic circular motions around the two spindle poles as well as the subtler counterrotating backflows between the posterior centrosomes and the cortices (see the insets in Fig. 3c,e). If both cytoplasmic and cortical pulling forces were present, then the resulting flows, and centrosome velocities, would be a linear combination of those shown in Fig. 3b,c (Supplementary Methods). Since, within experimental error, the measured flow agrees with the pattern observed in simulations of cortical pulling, with no sign of the complex flows predicted from cytoplasmic pulling, we estimate that the contributions from cortical pulling forces are manyfold greater than those from cytoplasmic pulling forces. Moreover, averaging the fluid flows at the peak of the oscillation  $(T_p)$  revealed no coherent fluid motions, in agreement with simulations for cortical

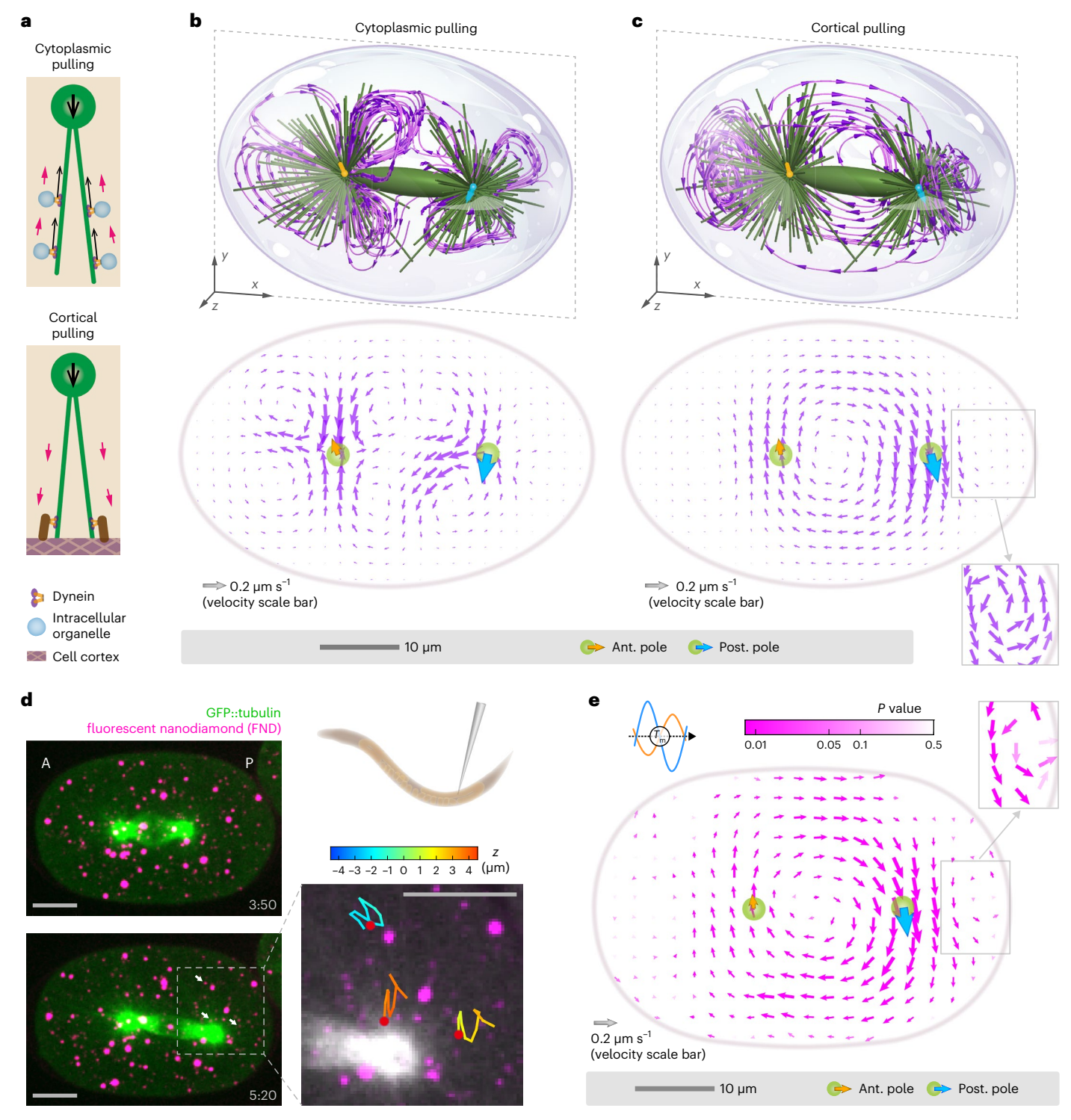


**Fig. 3** | **Fluid flows during spindle oscillations. a**, Schematic of fluid flow directions near a centrosome (green circle) and astral MTs (green lines). Top, in a cytoplasmic pulling model, the direction of fluid flow (magenta arrows) is opposite to that of centrosome motion (bold black arrow). Bottom, in a cortical pulling model, fluid flow and centrosome motion are in the same direction. **b,c**, Top panels, 3D computational fluid dynamics simulations near the midpoint of the oscillations at time  $T_m$  with cytoplasmic pulling (**b**) or cortical pulling (**c**). Bottom panels, averaged projections of the fluid vector fields onto the x-y planes of spindle motion from the above simulations. **d**, Left panels, two time frames ( $\Delta t$  = 90 s) of the maximal intensity projection of z-stack images with microinjected FNDs. Right, enlargement of the illustrative 50 s 3D trajectories of

FNDs (the three from the left image pointed out by white arrows), with their end locations marked by red dots. The z positions of the 3D trajectories are indicated by the colour bar. (All scale bars in **d** are 10  $\mu$ m.) **e**, Experimentally measured fluid flow vector field near the oscillation midpoint at time  $T_{\rm m}$  obtained by tracking FNDs from 20 embryos and averaging their projected x-y velocities. The length of the arrows is proportional to the flow velocity, and the colour indicates the statistical significance of the flow speed (P-value colour bar) (see Methods for details). Arrows on centrosomes indicate the mean measured centrosome velocities. The enlargements of the backflows in **c** and **e** are displayed with fixed-length vectors. Ant., anterior; Post., posterior.

pulling forces at that point in the oscillations and in strong disagreement with simulations for cytoplasmic pulling forces (Extended Data Fig. 3d-f). In sum, these results strongly suggest that the pulling forces acting on centrosomes during spindle oscillations are predominately cortically based.

# Cortical pulling positions in prometaphase and metaphase spindles

During the first mitotic division of *C. elegans* (Supplementary Video 1), the spindle forms near the cell centre and is aligned along the cell's long axis. The spindle remains centred in the prometaphase and the early metaphase, and slowly elongates towards the posterior in the late metaphase. We next investigated the nature of the forces acting on the spindle at these times.

We first used FESLA to test whether astral MTs exert pushing or pulling forces on the spindle when it is stably centred. Ablating rectangular planes either below (x-z) plane rectangular cuts, Fig. 4a) or posterior (y-z rectangular cuts, Fig. 4b) to the posterior centrosomes caused the centrosomes to immediately displace away from the cuts, suggesting that astral MTs in both directions exerted net pulling forces on the centrosomes (Supplementary Video 5). We next performed cups cuts, as described above, leaving only a cone of astral MTs associated with the centrosome emanating in either the transverse (Fig. 4c) or longitudinal (Fig. 4d) directions. In both cases, the centrosomes rapidly moved in the direction of the remaining astral MTs, displacing farther than in response to plane cuts and only slowing down once the astral MTs in the ablated regions had begun to recover (Supplementary Video 5). Thus, these experiments provide no sign of MT pushing forces, even when the centrosomes are displaced by ~5 µm towards the cell cortices, suggesting that pushing made a minimal contribution to the positioning forces near the cell centre (longer MTs push more weakly65).

We next used a combination of large-scale fluid dynamics simulations and measurements of fluid flow to determine whether the pulling forces that stably centre the spindle originate in the cytoplasm or at the cortex. Simulations of cytoplasmic pulling display extensive flows organized into vortices (Fig. 4e). Such large flows are necessarily present in a cytoplasmic pulling model, even when the spindle is stationary, as they are ultimately responsible for the forces that maintain the spindle position in this model. In contrast, flows only result from the motion of the spindle in a cortical pulling model, so are absent when the spindle is stationary (Fig. 4f). To experimentally measure the fluid flow when the spindle displayed no appreciable motion in the prometaphase, we tracked FNDs and averaged their trajectories together (Methods). No coherent fluid motion was present (Fig. 4g), consistent with the prediction of the cortical pulling model and inconsistent with cytoplasmic pulling.

We next investigated fluid flow during the slow spindle elongation in the metaphase when the posterior centrosome moves and the anterior centrosome is mostly stationary, before the onset of spindle oscillations. Simulations of the cytoplasmic pulling model (Fig. 4h) and cortical pulling model (Fig. 4i) produced distinct flows. Experimentally, averaging the trajectories of FNDs during spindle elongation in the metaphase (Methods) resulted in a flow pattern quite like the prediction of the cortical pulling model but inconsistent with the cytoplasmic pulling model (Fig. 4j). Since, within experimental error, the measured flow agrees with the pattern observed in simulations of cortical pulling, we estimate that the contributions to velocities from cortical pulling forces are manyfold greater than those from cytoplasmic pulling forces.

Taken together, through FESLA and by comparing fluid flow measurements with large-scale fluid dynamics simulations, we demonstrated that spindle positioning in the prometaphase and metaphase is primarily driven by cortical pulling forces, rather than from MT pushing or cytoplasmic pulling.

### Cortical pulling drives pronuclear centration and rotation

At an even earlier stage (Supplementary Video 1), the female and male pronuclei meet near the posterior cortex, and the PNC migrates towards the cell centre. During the centration process, the PNC rotates to align with the long axis of the cell centre. We next investigated the nature of the forces acting on the PNC.

We first used FESLA to test whether astral MTs exert pushing or pulling forces on the PNC. We separately probed astral MTs associated with the leading or trailing centrosomes by ablating rectangular planes near the centrosomes outside the pronuclei (Fig. 5a and Supplementary Video 6). In both cases, the centrosomes rapidly moved away from the cut astral MTs (Extended Data Fig. 4f,g), which is clearly seen by realigning the centrosomes relative to the cuts (Fig. 5b). These results imply that astral MTs primarily exert pulling forces on centrosomes during pronuclear centration. Simulations of cytoplasmic pulling during pronuclear rotation and centration produce a complex pattern of flows (Fig. 5c). In contrast, in both cortical pulling simulations (Fig. 5d and the inset) and FND-based measurements (Fig. 5e and the inset), the fluid rotates in conjunction with the PNC and contains a subtle backflow near the posterior centrosome.

Fluid flow measurements support cortical pulling but not cytoplasmic pulling. However, the MTs connecting the PNC to the anterior cortex cannot be clearly visualized<sup>48</sup>, and such MTs are necessary to support cortical pulling during pronuclear centration. We performed an additional test by cutting a large semicircular arc in front of the migrating PNC, close to the anterior cortex, such that only MTs a few micrometres away from the cortex would be ablated (Fig. 5f,g). The PNC immediately ceased advancing after the cutting (Fig. 5h and Supplementary Video 6), indicating that centration requires astral MTs to contact the anterior cortex. This result is not easily explained by a cytoplasmic pulling model but would be expected in a cortical pulling model. In sum, through FESLA and fluid flow analysis, we demonstrated that PNC migration is primarily driven by cortical pulling forces.

## Cortical pulling as an explanation for centrosome behaviours

Our above work shows that pulling forces always locally dominate (from FESLA) and these pulling forces result from cortical force generators (by comparing fluid flow measurements with large-scale fluid dynamics simulations) at all times in one-cell *C. elegans* embryos, namely during anaphase spindle oscillations, during metaphase and prometaphase stable positioning and during PNC centration. We next investigated whether cortical pulling forces alone are sufficient to account for these diverse centrosome motions. We developed a coarse-grained model derived from the biophysics of MT nucleation, growth and interaction with pulling cortical force generators (Supplementary Notes). In this model (Fig. 6a), a centrosome nucleates MTs at a rate  $\gamma$ , which grow from their plus-end with velocity  $V_{\rm g}$  and undergo a catastrophe<sup>46,52</sup> (that is, a switch from growing to shrinking) with rate  $\lambda$ . MTs that hit an unoccupied force generator bind to it and experience a pulling force  $f_0$ , which is transmitted to the centrosome. The force generators are stoichiometric. Each force generator can bind to at most one MT at a time<sup>39</sup>. Bound MTs detach from force generators at a rate  $\kappa$ , whereupon they undergo a catastrophe. MTs that hit the cell cortex without binding to a force generator undergo an immediate catastrophe. As in Fig. 6b, we consider a single centrosome moving along the y axis in a spherical cell of radius W, uniformly covered with M cortical force generators<sup>21,22,24,30,36,46,51,67</sup>. The net pulling force on the centrosome is the sum of pulling forces on all its MTs. This net pulling force is balanced by a drag force proportional to the centrosome's velocity (Supplementary Notes).

We first tested this model to see whether it is able to account for spindle oscillations. We numerically simulated the model using realistic parameters (Extended Data Table 1 and Extended Data Fig. 5)

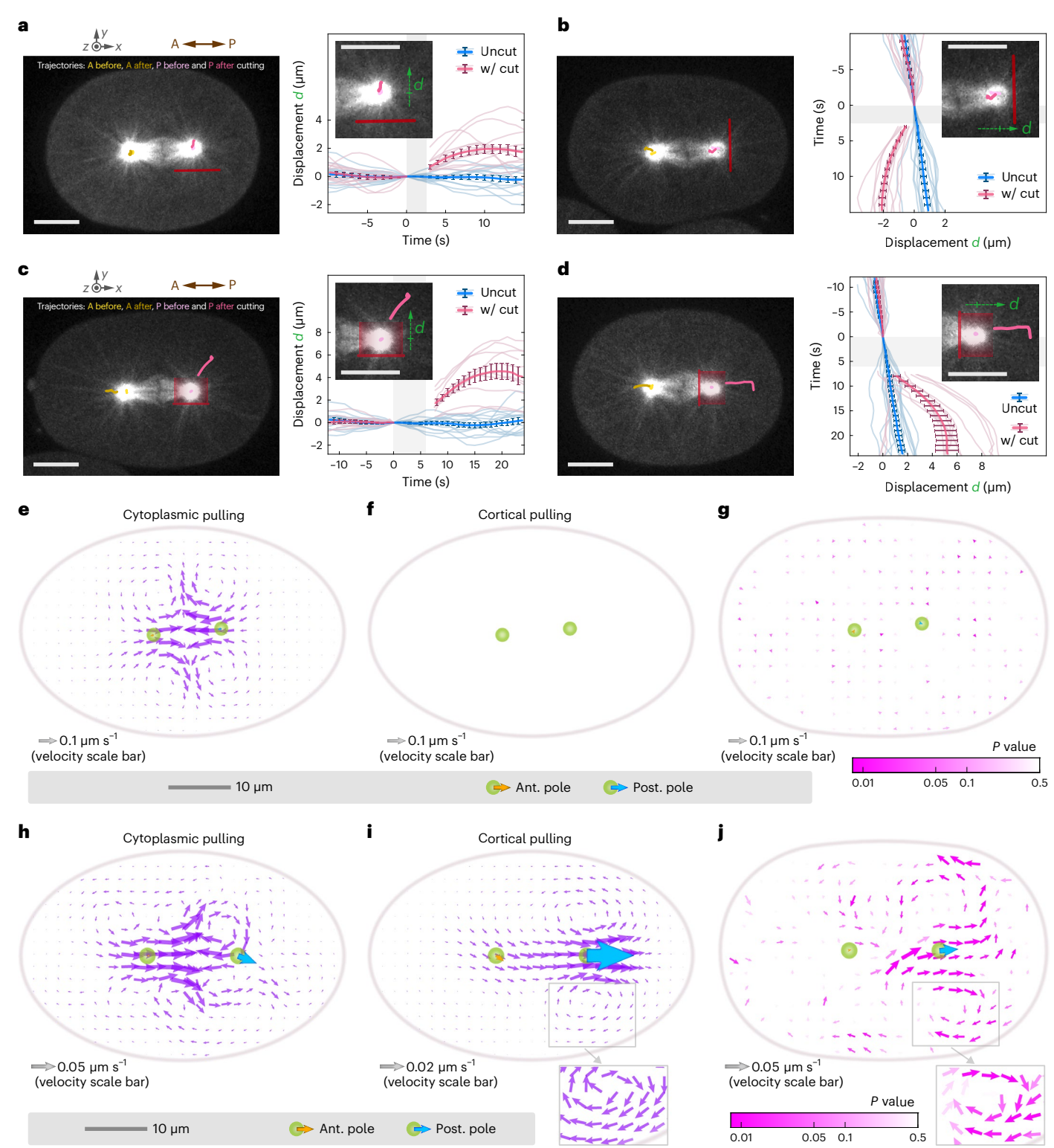


**Fig. 4** | **Laser ablation and fluid flows in prometaphase and metaphase.**  $\mathbf{a}$ - $\mathbf{d}$ , Laser ablation performed in metaphase (cutting patterns in red). The centrosome trajectories before and after cutting are plotted on the images with the designated colours. Right panels illustrate the corresponding definition of the displacement d in their insets and show the centrosome displacement data for uncut and cut embryos, with the mean value curves and SEM error bars overlaying the semitransparent raw data curves. All scale bars on images, including those of insets, are  $10~\mu m$ .  $\mathbf{a}$ , Rectangular (x-z) plane cuts on the transverse sides of the posterior centrosomes.  $\mathbf{b}$ , Rectangular (y-z) plane cuts located posteriorly to the posterior centrosomes.  $\mathbf{c}$ .  $\mathbf{d}$ , Cup cuts surrounding the posterior centrosomes with the opening mouths facing the transverse sides ( $\mathbf{c}$ ) or the posterior ends ( $\mathbf{d}$ ). See Extended Data Fig. 4a-d for the FESLA dimensions.

Sample numbers are  ${\bf a}$ , n=14 (uncut), n=14 (with cut);  ${\bf b}$ , n=14 (uncut), n=13 (with cut);  ${\bf c}$ , n=14 (uncut), n=10 (with cut) and  ${\bf d}$ , n=14 (uncut), n=14 (with cut).  ${\bf e}$ ,  ${\bf f}$ , Simulated fluid flows in prometaphase under ( ${\bf e}$ ) the cytoplasmic pulling or ( ${\bf f}$ ) the cortical pulling models.  ${\bf g}$ , The flow vector field of averaged experimental results from tracking FNDs in nine embryos in prometaphase.  ${\bf h}$ ,  ${\bf i}$ , Simulated fluid flows during spindle elongation in metaphase under ( ${\bf h}$ ) the cytoplasmic pulling or ( ${\bf i}$ ) the cortical pulling models.  ${\bf j}$ , Experimental flow vector field derived from averaging the movements of tracked FNDs in 14 embryos during spindle elongation in metaphase. The highlighted backflows in the enlargements in  ${\bf i}$  and  ${\bf j}$  are plotted with fixed-length vectors. The statistical significance of the velocity vectors is indicated by their colour scale (P-value colour bar) in  ${\bf g}$  and  ${\bf j}$ .

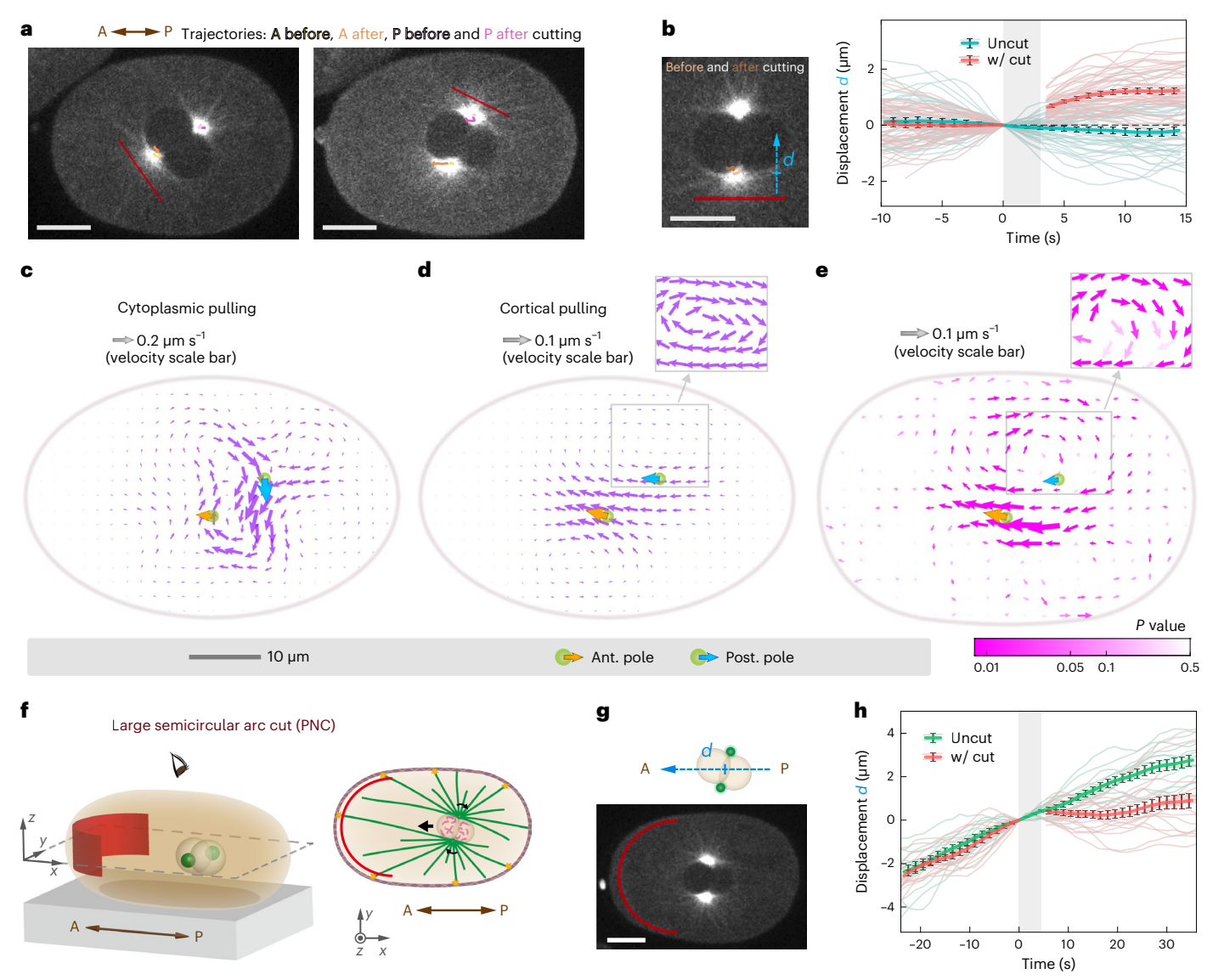


**Fig. 5** | **Laser ablation and fluid flows during migration of the PNC. a,b,** Rectangular plane cuts (ablation drawn in red) during PNC migration. **a,** Images indicating the locations of plane cuts. Left, cutting near the anterior or leading centrosome. Right, cutting near the posterior or trailing one. In both images, the centrosome trajectories within a window from 10 s before to 15 s after cutting are plotted. **b,** Left, the definition of the centrosome displacement d, which is the relative orthogonal (away from the cut) displacement from the locus right before cutting. Right, uncut (n = 48) and cut (n = 48) displacement data sets. **c,d,** Simulated fluid flows under (**c**) the cytoplasmic pulling or (**d**) the cortical pulling models. **e,** Experimental flow vector field obtained from averaging eight embryos with tracked FNDs. The statistical significance of the velocity vectors

is indicated by their colour scale (P-value colour bar). f-h, Large semicircular

arc cuts close to the anterior cortices during PNC migration.  ${\bf f}$ , 3D schematic (left) and 2D schematic (right) of the arc cut (drawn in red). The black arrows on the 2D schematic indicate PNC translation and rotation.  ${\bf g}$ , An image taken right after a semicircular arc cut. To quantify the progression of PNC migration, the displacement d is calculated by projecting the PNC centre onto the embryo long axis.  ${\bf h}$ , Migration displacements of uncut (n = 14) and cut (n = 19) embryos. For each ablated embryo, the zero point (d = 0) is defined by the PNC location right before cutting. All scale bars on images are 10  $\mu$ m. See Extended Data Fig. 4e,h for the FESLA dimensions. All displacement data are presented with mean value curves and SEM error bars overlaying the semitransparent raw data curves. In the enlargements in  ${\bf d}$  and  ${\bf e}$ , the highlighted circular flow patterns are displayed with fixed-length vectors.

during the anaphase and found that the centrosome oscillates with a similar amplitude and frequency to those seen experimentally (Fig. 6c). When the centrosome is at the top of the oscillations (Fig. 6d,  $t_1$ ), MTs are attached to force generators directly above the centrosome whereas force generators directly below the centrosome are largely unoccupied. MTs then start to attach to force generators below the centrosome, causing it to start moving downward (Fig. 6d,  $t_2$ ). More MTs continue to attach to the lower side and detach from the upper side (Fig. 6d,  $t_3$ ), and eventually, the process reverses (Fig. 6d,  $t_4$ ).

We gained further insights into the mechanism of oscillations from a linear stability analysis. A centrosome at the centre can lose stability to

an oscillatory state via a Hopf bifurcation if there is more than a critical number of cortical force generators, given by:

$$M_{\rm c} = \frac{3\eta \bar{\Omega}}{f_0 \bar{P}^2} \frac{V_{\rm g} W}{(\kappa W - 2V_{\rm g})}$$

where the steady-state rate of impingement of MTs onto force generators for a stationary centrosome at the cell centre before the start of oscillations is  $\bar{\Omega} \approx \frac{\gamma}{4} \left(\frac{r}{W}\right)^2 \exp(-W\lambda/V_{\rm g})$ ,  $\eta$  is the centrosome drag coefficient (including the associated astral MT array) and r is the capture radius of a force generator (which includes the distance over which a MT explores the cortex before binding). Here,  $\bar{P} = \bar{\Omega}/(\bar{\Omega} + \kappa)$ 

is the steady-state probability of a force generator being bound (Supplementary Notes). In this model, oscillations are only possible if

 $\frac{1}{\kappa} < \frac{W}{2V_{\rm g}}$ , that is, if the time a MT stays attached to a force generator is

sufficiently small compared to the time it takes for a MT to grow across the cell. Thus, the centrosome is driven to oscillate if pulling forces are sufficiently strong and the detachment of MTs from force generators is sufficiently fast.

These calculations and simulations point to an intuitive picture for how oscillations can occur with cortical pulling forces. Since the velocity of a growing MT plus-end is a sum of the MT's polymerization velocity in the direction of growth and the centrosome velocity (Fig. 6e)<sup>46</sup>, the motion of a centrosome away from a force generator reduces the rate of MT impingement on that force generator, whereas motion towards a force generator increases the rate of impingement. This results in a decreased probability of attachment and, hence, a decreased force from force generators behind the centrosome. It also results in an increased probability of attachment and, thus, an increased force in front of the centrosome. This self-reinforcing process move the centrosome over the midpoint (Y = 0). However, a forward-moving centrosome eventually reduces in speed due to a geometric effect. When the centrosome is closer to a surface, the force generators pulling it onwards do so from increasingly oblique angles, decreasing their pulling efficacy (Fig. 6f). Once the centrosome speed has slowed down, the MT impingement rate behind the centrosome gradually recovers, eventually stopping the centrosome. Then, MTs reattach to the force generators on the distal side of the centrosome, leading to a larger restoring force (because of the geometric effect) and, hence, oscillations. This phenomenology is robust to details of the system's geometry. The coarse-grained model also predicts that centrosome oscillations can occur between two flat plates.

One key assumption of the model is that MTs that contact the cortex undergo a catastrophe and depolymerize. Because of this effect, the simulations predict that the density of (transverse) MTs between the centrosome and the cortex oscillates out of phase with the centrosome's transverse position (Fig. 6g), which also occurs experimentally (Fig. 6h and Supplementary Video 7), supporting that MT depolymerization is induced upon contact with the cortex<sup>46</sup>.

We next investigated whether the cortical pulling forces are sufficient to explain the stable positioning of the spindle near the cell centre in the prometaphase and metaphase. If the number of cortical

force generators is reduced sufficiently in this model, then the centrosome ceases to oscillate and is stably centred (Supplementary Notes), which occurs due to a combination of the geometric effect described above (Fig. 6f) and the stoichiometric interactions between MTs and force generators. That is, each force generator can bind to at most one MT at a time<sup>39</sup>. In the absence of stoichiometric interactions, cortical pulling forces are always destabilizing and can never stably centre centrosomes (Supplementary Notes).

When the centrosome is stably centred, as in the prometaphase and metaphase, the resulting spring constant can be analytically calculated as (Supplementary Notes):

$$k_{\rm s} \approx \frac{2}{3} \frac{M f_0}{W} \bar{P}^2$$

Using the same parameters as those that reproduced anaphase spindle oscillations in the stochastic simulations but now lowering only M, the number of cortical force generators, this simulation gives a spring constant for spindle centring of 4.8 pN µm<sup>-1</sup> (Extended Data Fig. 5b), which is the same order of magnitude as the measurements of Garzon-Coral et al.  $(16.4 \pm 2.1 \, pN \, \mu m^{-1})^{16}$ . Therefore, a model with only cortical pulling forces is sufficient to explain the stable centring of the spindle in the prometaphase and metaphase. A reduction in the number of cortical force generators in the prometaphase and metaphase compared to the anaphase is consistent with the ablation of astral MTs causing more dramatic motions in the anaphase (compare Fig. 1 and Fig. 4) and conclusions from previous studies 14,30,35,37,54-56. The predicted transition between oscillations and stable positioning upon changing the number of cortical force generators can also account for the observation that gpr-1/2 knockdown prevents oscillations<sup>21</sup>.

We next investigated whether cortical pulling forces are sufficient to explain the PNC centration process. We used the same cortical pulling model that reproduced the anaphase oscillations and stable centring in the prometaphase and metaphase and assumed that there was the same number of cortical force generators as in the prometaphase and metaphase. The coarse-grained theory can be used to analytically calculate (Supplementary Notes) that the PNC should exponentially approach the centre with a timescale  $\tau_c$  given by:

$$\frac{1}{\tau_{\rm c}} = \frac{1}{2} \left( \bar{\Omega} + \kappa \right) \left( 1 - \frac{M}{M_{\rm c}} \right)$$

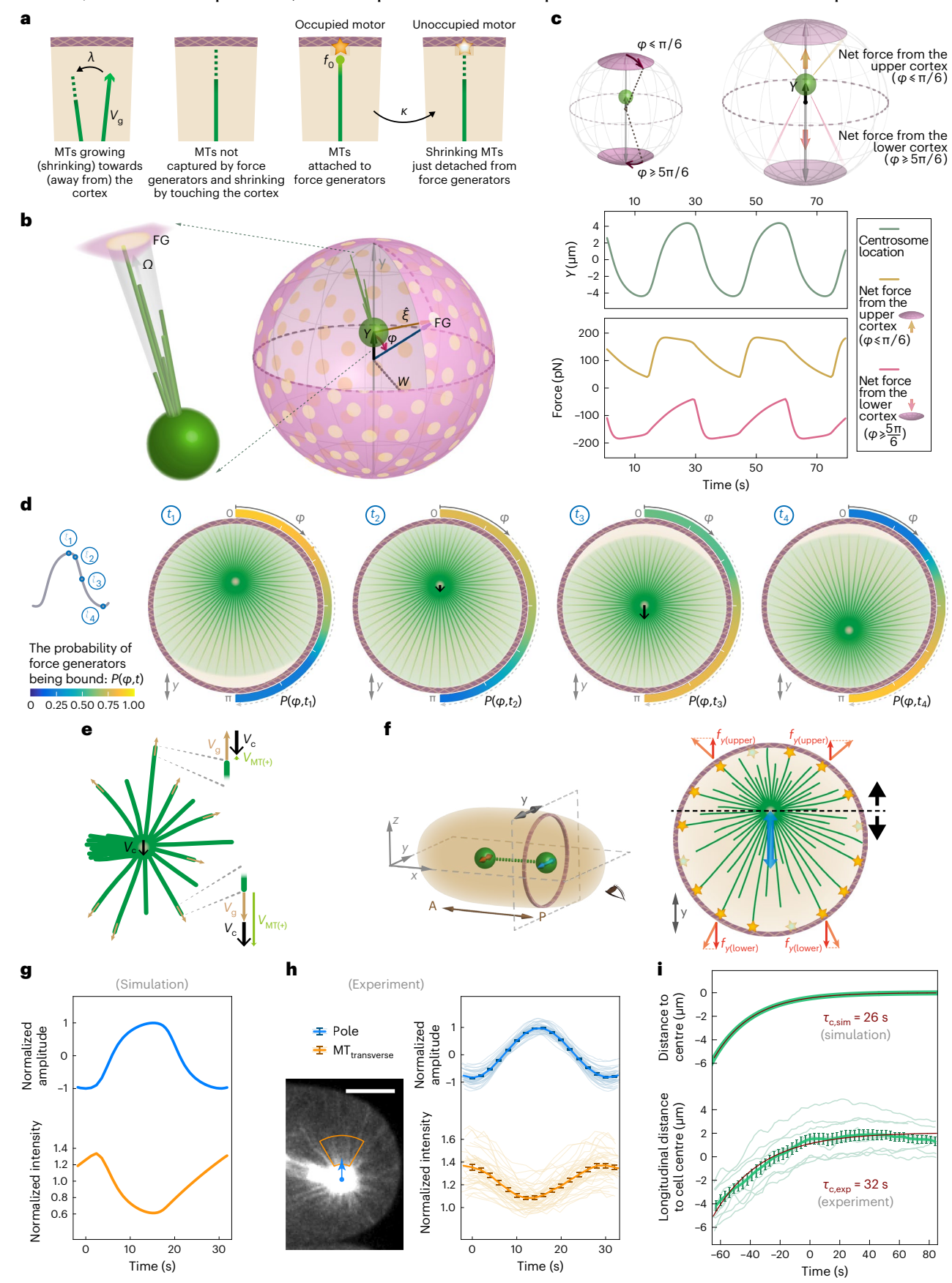
### **Fig. 6** | **Coarse-grained model of cortical pulling and model predictions. a**, Key processes in the coarse-grained model. From left to right, MTs grow from

their plus-ends with velocity  $V_g$  and undergo a catastrophe (that is, a switch from growing to shrinking) with rate  $\lambda$ . MTs that hit the cell cortex without binding to a force generator undergo an immediate catastrophe. MTs that hit an unoccupied force generator bind to it and experience a pulling force  $f_0$ . Bound MTs detach from force generators at a rate  $\kappa$ , whereupon they undergo a catastrophe. **b**, Geometry of the coarse-grained model. The cell is treated as a sphere of radius  $\it W$  decorated with force generators (FG, yellow discs). The centrosome (green sphere) is located at a distance Y (along the y axis) from the centre of the cell.  $\hat{\xi}$  is a unit vector extending from the centrosome to an FG.  $\Omega$  is the impingement rate of MTs onto a FG. c, To illustrate the mechanism of oscillations, it is helpful to investigate the forces exerted on the centrosome from small regions (polar caps) above and below the centrosomes (upper schematic). The plots show the simulated oscillation amplitude and the net cortical forces from FGs in these polar cap regions. Note that in the simulations, all astral MTs bound to force generators exert forces on the centrosomes (that is, not just those in the polar cap regions). d, From a simulation of oscillations with the coarse-grained model, the probability of a cortical force generator being bound is  $P(\varphi, t)$ , which is a function of polar angle  $\varphi$  from the y axis and time, as displayed by the colour scale in the bottom colour bar. This information is expressed for a cross section through the sphere containing the yaxis. The black arrows drawn on centrosomes indicate their velocities. The green field shows the centrosomal

MT directions and the front of unattached plus-ends. e, Relations among the centrosome speed  $V_c$ , the MT growth (polymerization) speed  $V_g$  and the speeds of MT plus-ends  $V_{\text{MT}(+)}$ . **f**, Schematic of the geometric effects that lead to the restoring mechanism during oscillations. Viewed from the embryo posterior end, the centrosome oscillates along the y direction on the y-z plane (right panel). As the centrosome approaches the upper surface, the forces from FGs above the centrosome become more oblique, leading to a smaller upward force projected along the yaxis.  $\mathbf{g}$ - $\mathbf{i}$ , Theoretical predictions and experimental measurements of  $a stral\,MT\,density\,and\,pronuclear\,centration.\,\textbf{g}, The\,simulation\,predicted\,that\,the$ density of astral MTs (lower, yellow curve) within an annular sector along the transverse direction oscillates out of phase with the transverse position of the centrosome (upper, blue curve). h, Experimental measurement of the centrosomes' transverse amplitudes and the intensities of astral MTs within annular sectors (60°, 3  $\mu m$  inner radius, 9  $\mu m$  outer radius, as the yellow frame on the image) of the transverse directions. Altogether, 44 oscillation cycles were extracted from 11 embryos (Methods). Scale bar, 10 um. i. The simulated (upper) and experimental (lower, n = 10) results of pronuclear centration with exponential fits (dark red curves) and the resulting centring timescales  $\tau_{c,sim}$  and  $\tau_{\rm c.exp}$ . The distance is calculated from the centrosome to the sphere centre in simulations, and experimentally from the PNC centre to the embryo centre along the longitudinal direction. Experimental data in **h** and **i** are presented with mean value curves and SEM error bars overlaying the semitransparent raw data curves.

Consistent with this prediction, exponential relaxation was observed in both simulations and experiments (Fig. 6i and Extended Data Fig. 5a), with timescales of 26 and 32 s, respectively (95% confidence interval, 29–36 s in our experiments). A second prediction of

the coarse-grained theory is that the centring timescale  $\tau_c$  is the same as the timescale  $\tau_c$  of approach to a new equilibrium in response to an applied force. Consistent with this prediction, the observed centring times quoted above are the same as the force response timescale found



in simulations of the coarse-grain model,  $\tau_{f,\text{sim}} = 25 \text{ s}$ , and previously experimentally measured  $\tau_{f,\text{exp}} = 28 \text{ s}$  (95% confidence interval, 26–31 s, from Supplementary Fig. 13 in Garzon-Coral et al. <sup>16</sup>).

#### Conclusion

We have shown that cortical pulling forces drive pronuclear migration and rotation as well as spindle centring, elongation and oscillations in *C. elegans* embryos, with no discernible contribution from MT pushing or cytoplasmic pulling forces. This was accomplished using a combination of FESLA (to distinguish between pushing and pulling), fluid flow analysis (to differentiate between cytoplasmic and cortical pulling) and coarse-grained modelling. Previous work demonstrated that the asymmetric positioning of the spindle can also be explained by cortical pulling forces<sup>39</sup>. Thus, cortical pulling forces are sufficient to drive the diverse cell biological behaviour of centrosomes including directed motions, stable positioning and oscillations. Since such centrosome behaviours are observed in diverse contexts<sup>7,12–20</sup>, as are cortical pulling forces<sup>38</sup>, the principles we have uncovered here should be broadly applicable to other systems.

#### Online content

Any methods, additional references, Nature Portfolio reporting summaries, source data, extended data, supplementary information, acknowledgements, peer review information; details of author contributions and competing interests; and statements of data and code availability are available at https://doi.org/10.1038/s41567-023-02223-z.

#### References

- Knoblich, J. A. Asymmetric cell division: recent developments and their implications for tumour biology. *Nat. Rev. Mol. Cell Biol.* 11, 849–860 (2010).
- Kotak, S., Busso, C. & Gönczy, P. Cortical dynein is critical for proper spindle positioning in human cells. J. Cell Biol. 199, 97–110 (2012).
- Siller, K. H. & Doe, C. Q. Spindle orientation during asymmetric cell division. Nat. Cell Biol. 11, 365–374 (2009).
- Kiyomitsu, T. & Cheeseman, I. M. Chromosome- and spindle-pole-derived signals generate an intrinsic code for spindle position and orientation. *Nat. Cell Biol.* 14, 311–317 (2012).
- Pearson, C. G. & Bloom, K. Dynamic microtubules lead the way for spindle positioning. Nat. Rev. Mol. Cell Biol. 5, 481–492 (2004).
- Tame, M. A. et al. Astral microtubules control redistribution of dynein at the cell cortex to facilitate spindle positioning. *Cell Cycle* 13, 1162–1170 (2014).
- von Dassow, G., Verbrugghe, K. J., Miller, A. L., Sider, J. R. & Bement, W. M. Action at a distance during cytokinesis. J. Cell Biol. 187, 831–845 (2009).
- Minc, N., Burgess, D. & Chang, F. Influence of cell geometry on division-plane positioning. Cell 144, 414–426 (2011).
- Reinsch, S. & Gonczy, P. Mechanisms of nuclear positioning— Commentary. J. Cell Sci. 111, 2283–2295 (1998).
- Reinsch, S. & Karsenti, E. Movement of nuclei along microtubules in Xenopus egg extracts. Curr. Biol. 7, 211–214 (1997).
- Rujano, M. A., Sanchez-Pulido, L., Pennetier, C., le Dez, G. & Basto, R. The microcephaly protein Asp regulates neuroepithelium morphogenesis by controlling the spatial distribution of myosin II. Nat. Cell Biol. 15, 1294–1306 (2013).
- Longo, F. J. & Anderson, E. The fine structure of pronuclear development and fusion in the sea urchin, *Arbacia punctulata*. J. Cell Biol. 39, 339–368 (1968).
- Meaders, J. L. & Burgess, D. R. Microtubule-based mechanisms of pronuclear positioning. Cells 9, 505 (2020).
- 14. Cowan, C. R. & Hyman, A. A. Asymmetric cell division in *C. elegans*: cortical polarity and spindle positioning. *Annu. Rev. Cell Dev. Biol.* **20**, 427–453 (2004).

- Tanimoto, H., Sallé, J., Dodin, L. & Minc, N. Physical forces determining the persistency and centring precision of microtubule asters. *Nat. Phys.* 14, 848–854 (2018).
- Garzon-Coral, C., Fantana, H. A. & Howard, J. A force-generating machinery maintains the spindle at the cell center during mitosis. Science 352, 1124–1127 (2016).
- 17. Foe, V. E. & von Dassow, G. Stable and dynamic microtubules coordinately shape the myosin activation zone during cytokinetic furrow formation. *J. Cell Biol.* **183**, 457–470 (2008).
- Du, Q. & Macara, I. G. Mammalian Pins is a conformational switch that links NuMA to heterotrimeric G proteins. Cell 119, 503–516 (2004).
- Riche, S. et al. Evolutionary comparisons reveal a positional switch for spindle pole oscillations in *Caenorhabditis* embryos. J. Cell Biol. 201, 653–662 (2013).
- Zhu, M. et al. MISP is a novel Plk1 substrate required for proper spindle orientation and mitotic progression. J. Cell Biol. 200, 773–787 (2013).
- Pecreaux, J. et al. Spindle oscillations during asymmetric cell division require a threshold number of active cortical force generators. Curr. Biol. 16, 2111–2122 (2006).
- Grill, S. W., Kruse, K. & Jülicher, F. Theory of mitotic spindle oscillations. *Phys. Rev. Lett.* 94, 108104 (2005).
- Grill, S. W., Gonczy, P., Stelzer, E. H. & Hyman, A. A. Polarity controls forces governing asymmetric spindle positioning in the Caenorhabditis elegans embryo. Nature 409, 630–633 (2001).
- Grill, S. W., Howard, J., Schaffer, E., Stelzer, E. H. & Hyman, A. A. The distribution of active force generators controls mitotic spindle position. *Science* 301, 518–521 (2003).
- Bellanger, J. M. et al. ZYG-9, TAC-1 and ZYG-8 together ensure correct microtubule function throughout the cell cycle of C. elegans embryos. J. Cell Sci. 12016, 2963–2973 (2007).
- 26. Hyman, A. A. & White, J. G. Determination of cell division axes in the early embryogenesis of *Caenorhabditis elegans*. *J. Cell Biol.* **105**, 2123–2135 (1987).
- 27. Le Bot, N., Tsai, M. C., Andrews, R. K. & Ahringer, J. TAC-1, a regulator of microtubule length in the *C. elegans* embryo. *Curr. Biol.* **13**, 1499–1505 (2003).
- Srayko, M., Quintin, S., Schwager, A. & Hyman, A. A. Caenorhabditis elegans TAC-1 and ZYG-9 form a complex that is essential for long astral and spindle microtubules. Curr. Biol. 13, 1506–1511 (2003).
- 29. Wright, A. J. & Hunter, C. P. Mutations in a  $\beta$ -tubulin disrupt spindle orientation and microtubule dynamics in the early *Caenorhabditis* elegans embryo. *Mol. Biol. Cell* **14**, 4512–4525 (2003).
- Colombo, K. et al. Translation of polarity cues into asymmetric spindle positioning in *Caenorhabditis elegans* embryos. *Science* 300, 1957–1961 (2003).
- Bringmann, H., Cowan, C. R., Kong, J. & Hyman, A. A. LET-99, GOA-1/GPA-16, and GPR-1/2 are required for aster-positioned cytokinesis. Curr. Biol. 17, 185–191 (2007).
- Goulding, M. B., Canman, J. C., Senning, E. N., Marcus, A. H. & Bowerman, B. Control of nuclear centration in the C. elegans zygote by receptor-independent Ga signaling and myosin II. J. Cell Biol. 178, 1177–1191 (2007).
- 33. Galli, M. et al. aPKC phosphorylates NuMA-related LIN-5 to position the mitotic spindle during asymmetric division. *Nat. Cell Biol.* **13**, 1132–1138 (2011).
- Tsou, M. F., Hayashi, A., DeBella, L. R., McGrath, G. & Rose, L. S. LET-99 determines spindle position and is asymmetrically enriched in response to PAR polarity cues in C. elegans embryos. Development 129, 4469–4481 (2002).
- Nguyen-Ngoc, T., Afshar, K. & Gonczy, P. Coupling of cortical dynein and Ga proteins mediates spindle positioning in Caenorhabditis elegans. Nat. Cell Biol. 9, 1294–1302 (2007).

- Krueger, L. E., Wu, J. C., Tsou, M. F. & Rose, L. S. LET-99 inhibits lateral posterior pulling forces during asymmetric spindle elongation in *C. elegans* embryos. *J. Cell Biol.* 189, 481–495 (2010).
- Gotta, M., Dong, Y., Peterson, Y. K., Lanier, S. M. & Ahringer, J. Asymmetrically distributed C. elegans homologs of AGS3/ PINS control spindle position in the early embryo. Curr. Biol. 13, 1029–1037 (2003).
- Wu, H.-Y., Nazockdast, E., Shelley, M. J. & Needleman, D. J. Forces positioning the mitotic spindle: theories, and now experiments. *BioEssays* 39, 1600212 (2017).
- Farhadifar, R. et al. Stoichiometric interactions explain spindle dynamics and scaling across 100 million years of nematode evolution. eLife 9, e55877 (2020).
- Yu, C.-H. et al. Central-spindle microtubules are strongly coupled to chromosomes during both anaphase A and anaphase B. Mol. Biol. Cell 30, 2503–2514 (2019).
- 41. Chung, S. H., Clark, D. A., Gabel, C. V., Mazur, E. & Samuel, A. D. The role of the AFD neuron in *C. elegans* thermotaxis analyzed using femtosecond laser ablation. *BMC Neurosci.* **7**, 30 (2006).
- 42. Chung, S. H. & Mazur, E. Surgical applications of femtosecond lasers. *J. Biophotonics* **2**, 557–572 (2009).
- 43. Gabel, C. V., Antoine, F., Chuang, C.-F., Samuel, A. D. & Chang, C. Distinct cellular and molecular mechanisms mediate initial axon development and adult-stage axon regeneration in *C. elegans*. *Development* **135**, 1129–1136 (2008).
- 44. Gabel, C. V. et al. Neural circuits mediate electrosensory behavior in *Caenorhabditis elegans*. *J. Neurosci.* **27**, 7586–7596 (2007).
- Vogel, A., Noack, J., Hüttman, G. & Paltauf, G. Mechanisms of femtosecond laser nanosurgery of cells and tissues. *Appl. Phys. B* 81, 1015–1047 (2005).
- Kozlowski, C., Srayko, M. & Nedelec, F. Cortical microtubule contacts position the spindle in *C. elegans* embryos. *Cell* 129, 499–510 (2007).
- Kimura, A. & Onami, S. Computer simulations and image processing reveal length-dependent pulling force as the primary mechanism for *C. elegans* male pronuclear migration. *Dev. Cell* 8, 765–775 (2005).
- 48. Kimura, K. & Kimura, A. Intracellular organelles mediate cytoplasmic pulling force for centrosome centration in the *Caenorhabditis elegans* early embryo. *Proc. Natl Acad. Sci. USA* **108**, 137–142 (2011).
- 49. Shinar, T., Mana, M., Piano, F. & Shelley, M. J. A model of cytoplasmically driven microtubule-based motion in the single-celled *Caenorhabditis elegans* embryo. *Proc. Natl Acad.* Sci. USA **108**, 10508–10513 (2011).
- Xie, J. & Minc, N. Cytoskeleton force exertion in bulk cytoplasm. Front. Cell Dev. Biol. https://doi.org/10.3389/fcell.2020.00069 (2020).
- 51. Gusnowski, E. M. & Srayko, M. Visualization of dynein-dependent microtubule gliding at the cell cortex: implications for spindle positioning. *J. Cell Biol.* **194**, 377–386 (2011).
- Laan, L. et al. Cortical dynein controls microtubule dynamics to generate pulling forces that position microtubule asters. *Cell* 148, 502–514 (2012).

- 53. Redemann, S. et al. Membrane invaginations reveal cortical sites that pull on mitotic spindles in one-cell *C. elegans* embryos. *PLoS ONE* **5**, e12301 (2010).
- 54. Schmidt, R. et al. Two populations of cytoplasmic dynein contribute to spindle positioning in *C. elegans* embryos. *J. Cell Biol.* **216**, 2777–2793 (2017).
- 55. Srinivasan, D. G., Fisk, R. M., Xu, H. & van den Heuvel, S. A complex of LIN-5 and GPR proteins regulates G protein signaling and spindle function in C. elegans. Genes Dev. 17, 1225–1239 (2003).
- Couwenbergs, C. et al. Heterotrimeric G protein signaling functions with dynein to promote spindle positioning in C. elegans. J. Cell Biol. 179, 15–22 (2007).
- 57. Daniels, B. R., Masi, B. C. & Wirtz, D. Probing single-cell micromechanics in vivo: the microrheology of *C. elegans* developing embryos. *Biophys. J.* **90**, 4712–4719 (2006).
- 58. Valentine, M. T. et al. Colloid surface chemistry critically affects multiple particle tracking measurements of biomaterials. *Biophys. J.* **86**, 4004–4014 (2004).
- Mochalin, V. N., Shenderova, O., Ho, D. & Gogotsi, Y. The properties and applications of nanodiamonds. *Nat. Nanotechnol.* 7, 11–23 (2012).
- Fu, C.-C. et al. Characterization and application of single fluorescent nanodiamonds as cellular biomarkers. *Proc. Natl Acad. Sci. USA* 104, 727–732 (2007).
- 61. Mohan, N., Chen, C.-S., Hsieh, H.-H., Wu, Y.-C. & Chang, H.-C. In vivo imaging and toxicity assessments of fluorescent nanodiamonds in *Caenorhabditis elegans. Nano Lett.* **10**, 3692–3699 (2010).
- 62. Vaijayanthimala, V. et al. The long-term stability and biocompatibility of fluorescent nanodiamond as an in vivo contrast agent. *Biomaterials* **33**, 7794–7802 (2012).
- 63. Chang, Y.-R. et al. Mass production and dynamic imaging of fluorescent nanodiamonds. *Nat. Nanotechnol.* **3**, 284–288 (2008).
- 64. Su, L.-J. et al. Fluorescent nanodiamonds enable quantitative tracking of human mesenchymal stem cells in miniature pigs. *Sci. Rep.* **7**, 45607 (2017).
- 65. Howard, J. Mechanics of motor proteins and the cytoskeleton. *Appl. Mech. Rev.* **55**, B39 (2002).
- 66. Coffman, V. C., McDermott, M. B., Shtylla, B. & Dawes, A. T. Stronger net posterior cortical forces and asymmetric microtubule arrays produce simultaneous centration and rotation of the pronuclear complex in the early *Caenorhabditis elegans* embryo. *Mol. Biol. Cell* 27, 3550–3562 (2016).
- 67. Grill, S. W. & Hyman, A. A. Spindle positioning by cortical pulling forces. *Dev. Cell* **8**, 461–465 (2005).

**Publisher's note** Springer Nature remains neutral with regard to jurisdictional claims in published maps and institutional affiliations.

Springer Nature or its licensor (e.g. a society or other partner) holds exclusive rights to this article under a publishing agreement with the author(s) or other rightsholder(s); author self-archiving of the accepted manuscript version of this article is solely governed by the terms of such publishing agreement and applicable law.

@ The Author(s), under exclusive licence to Springer Nature Limited 2023

#### Methods

#### **Experimental subjects**

Worm strains. The *C. elegans* line *AZ244* (unc-119(ed3) III; ruls57[unc-119(+) pie-1::GFP::tubulin]) and a new line *DJN004* (unc-119(ed3) III; ruls57[unc-119(+) pie-1::GFP::tubulin; [mCherry::tbg-1]) obtained by crossing *AZ244* with a line expressing mCherry-labelled γ-tubulin were used throughout this study. Additionally, to visualize chromosomes, *SA250* (tjls54 [pie-1p::GFP::tbb-2+ pie-1p::2xmCherry::tbg-1+ unc-119(+)]; tjls57 [pie-1p::mCherry::his-48+ unc-119(+)]) were used for the metaphase experiments shown in Fig. 4a–d. This line helped to determine the timing of the metaphase and ensure that the chromosomes were not ablated.

*C. elegans* culturing conditions and embryo preparation. Worms were grown on nematode growth medium plates seeded with OP50 *Escherichia coli* bacteria and incubated at 24 °C. Gravid *C. elegans* hermaphrodites were dissected by needle tips to release their embryos into M9 buffer. Then, mouth pipettes were used to pick and transfer early embryos onto flat 4% agarose pads (Bio-Rad), which were prepared on microscopic slides<sup>68</sup>. A freshly made agarose pad was promptly trimmed to a size smaller than the area of a coverslip. After adding a small amount of M9 buffer to keep the embryos moist, the sample was covered with a coverslip and sealed swiftly for imaging. Under this mounting condition, embryos were slightly squeezed and were held in place by the sunk agarose pad.

After the embryos were prepared, they were imaged either at 22 °C or 18 °C. For different laser-ablation conditions, each set of embryos, including both control uncut and ablated embryos, were imaged at the same temperature for comparison (either all at 22 °C or all at 18 °C).

#### **Experimental methods**

**Microscopy and imaging.** We imaged mounted early *C. elegans* embryos on an inverted microscope (Nikon, TE2000) using a ×60 water-immersion objective (Nikon, CFI Plan Apo VC 60X WI, NA 1.2). Images were acquired using a spinning-disc confocal unit (Yokugawa, CSU-XI) equipped with continuous-wave lasers for fluorescence excitation and an electron-multiplying charge-coupled device (Hamamatsu, ImagEM Enhanced C9100-13) for detection. GFP fluorescence was excited at 488 nm and collected through a bandpass filter with 514 nm centre and 30 nm full width at half maximum (FWHM) wavelength. mCherry fluorescence was excited at 561 nm and collected through a bandpass filter with 593 nm centre and 40 nm FWHM wavelength. The FNDs were excited at 561 nm and collected through a long-pass filter with a 647 nm cut-on wavelength.

All images displayed in the figures and videos in this article were processed in MATLAB (MathWorks) or ImageJ.

Extended Data Fig. 1a indicates the terminology for embryo orientation and axis labels used throughout this manuscript. The x-y midplane is defined as the imaging plane. The longitudinal direction (or the long axis) of an oblong embryo is assigned as the x direction, whereas the transverse direction is in the y direction.

Femtosecond stereotactic laser ablation. Our laser-ablation setup was incorporated into an inverted microscope with a spinning-disc unit (Fig. 1c). A near-infrared Ti:sapphire femtosecond pulsed laser beam with a reduced repetition rate (16–80 kHz, compared to the common 80 MHz repetition rate output)<sup>41–45</sup> was directed and merged into the microscope light path through a dichroic mirror. The ablation laser pulses were focused onto the sample by the same high-numerical-aperture objective used for confocal imaging. We used two different methods to reduce the repetition rate of the femtosecond laser pulses: (1) Using a cavity-dumped Ti:sapphire laser (Cascade-1, KML, with 830–840 nm centre wavelength and 20–30 fs pulse width) with either a 40 kHz pulse train with 2.5–4 nJ pulse energy (the energy measured under our ×60 water-immersion objective) or an 80 kHz

pulse train with 2.5–3.5 nJ pulse energy. (2) Using a pulse picker (Eclipse, KMLabs) to select a 16 kHz pulse train from the 80 MHz Ti:sapphire laser pulses (Mai-Tai, Spectra-Physics, with 800 nm centre wavelength and -70 fs pulse width).

We ablated complex patterns by moving the sample on a three-axis piezo-stage (P-545 Plnano XYZ, Physik Instrumente) and controlling laser exposure with a fast mechanical shutter (Newport). Ablation patterns and image acquisition were controlled with custom LabVIEW codes. The dimensions of the FESLA ablated regions are displayed in extended data figures: (1) For experiments during the late metaphase to anaphase spindle oscillations, see Extended Data Fig. 2a (for arc cuts in Fig. 1e–j), Extended Data Fig. 2e (for double rectangular plane cuts), Extended Data Fig. 2f (for open-cylindrical cuts in Fig. 2a–e) and Extended Data Fig. 2i (for cup cuts in Fig. 2f–i). (2) For experiments during the metaphase, see Extended Data Fig. 4a,b (for rectangular plane cuts in Fig. 4a,b) and Extended Data Fig. 4c,d (for cup cuts in Fig. 4c,d). (3) For experiments during the PNC stage, see Extended Data Fig. 4e (for rectangular plane cuts in Fig. 5a,b) and Extended Data Fig. 4h (for large semicircular arc cuts in Fig. 5f–h).

Fluorescent nanodiamonds. Passivated FNDs were used as tracer particles to visualize cytoplasmic flows. We adopted a two-step surface treatment to coat FNDs with mono-methyl polyethylene glycol (mPEG). FNDs (40–50 nm in diameter, after acid wash treatment, a gift from Dr Huan-Cheng Chang)60-62,64 in Milli-Q water were sonicated for 30 min and then mixed with  $\alpha$ -lactal burnin (Sigma,  $\alpha$ -lactal burnin from calcium-depleted bovine milk) at a weight ratio of FND:α-lactal bumin of 1:2. The mixture was gently shaken overnight at 4 °C, and then washed through a centrifugal filter (Amicon Ultra, 100 kDa) several times. The FND concentrate was dispersed in Milli-Q water again and sonicated in ice water bath for 15 min and then optionally syringe filtered (Millex-VV, 0.1 µm, Durapore polyvinylidene fluoride membrane). After diluting the solution of FND (with absorbed α-lactalbumin) to ~0.1 mg ml<sup>-1</sup>, boric acid was added to reach a final concentration of 5 mM and the pH was adjusted to 8. For the second mPEG coating, fresh mPEG-SVA (mPEG-succinimidyl valerate, mol. wt. 5,000, Laysan Bio) was added to a weight ratio of FND: mPEG-SVA ≈ 1:1, and the mixture was stirred overnight at 4 °C. Then, the FNDs were washed through a centrifugal filter several times and dispersed in Milli-Q water. Immediately before use, the FND solution was sonicated in an ice water bath for 15 min, syringe filtered (Pall Acrodisc, 0.2 um, HT Tuffryn membrane) and diluted to a concentration of 0.25-1 mg ml<sup>-1</sup>.

We microinjected freshly coated FNDs (within 48 h) into the distal gonads of *AZ244* (unc-119(ed3) III; ruls57[unc-119(+) pie-1::GFP::tubulin]) young adult hermaphrodites using needles pulled from borosilicate glass capillaries (World Precision Instruments, 1.0 mm outer diameter, 0.58 mm internal diameter, with filament) with a P-87 micropipette puller (Sutter Instrument). We cut the hermaphrodites 6–10 h after microinjection and retrieved their embryos for imaging.

We imaged AZ244 embryos with injected FNDs at  $18\,^{\circ}$ C. Time-lapse z-stack confocal images of both GFP:: $\beta$ -tubulin and FND were acquired every  $2.5-5\,\text{s}$ . Centrosomes were visualized in GFP:: $\beta$ -tubulin images, which included several z sections with  $1\,\mu\text{m}$  spacing and were taken around PNCs or spindles. FND signals were captured through z stacks having  $9\,\text{or}\,15\,\text{z}\,\text{section}$  images with  $1\,\mu\text{m}\,\text{spacing}$ .

#### Quantification and data analysis

All image analyses and data quantification for experimental data were done in MATLAB (MathWorks). Numerical simulations and their analyses were also done in MATLAB.

**Tracking centrosomes.** The locations of centrosomes were extracted from either fluorescent  $\gamma$ -tubulin or fluorescent  $\beta$ -tubulin (Extended Data Fig. 1b). For  $\gamma$ -tubulin images (Extended Data Fig. 1b, upper right), we adopted the particle-finding codes from the MATLAB Particle

Tracking Code Repository by D. Blair and E. Dufresne (http://site.physics.georgetown.edu/matlab/) (adapted from IDL Particle Tracking software from David D. Grier, John C. Crocker and Eric R. Weeks)<sup>69</sup> to find the centrosome locations. We used high-pass background subtraction followed by thresholding and identification of local maxima. Subpixel localization of the anterior and posterior centrosomes (orange and blue circles on the upper right image of Extended Data Fig. 1b) was achieved by calculating the centroid near the identified local maximum. For β-tubulin images, the tracking algorithm described above worked well at the PNC stage, but the complex appearance of spindle centrosomes (Extended Data Fig. 1b, lower right image) necessitated an alternative approach. In this case, we used an image-correlation-based approach. We constructed a square region with an artificial ring with a size close to that of a centrosome (Extended Data Fig. 1c. upper), convolved this 'synthetic' centrosome against background-subtracted and thresholded images of spindles (Extended Data Fig. 1c, lower) and identified the position of centrosomes as the local maximum of this correlation (labelled with circles in Extended Data Fig. 1b, lower right image). After acquiring the locations of the centrosomes in each frame (for either  $\gamma$ -tubulin or  $\beta$ -tubulin imaging), we then used the tracking routines from the MATLAB Particle Tracking Code Repository to link these positions into trajectories.

During centrosome oscillations, we defined the longitudinal direction of motion to be along the best-fitting straight line to the combined trajectories of the two centrosomes (Extended Data Fig. 1d). During the metaphase and the PNC stage and for certain ablation data during the oscillations, we instead defined the longitudinal direction of motion by an embryo's geometry. We determined the cell boundary by thresholding (and smoothing) the  $\beta$ -tubulin image (Extended Data Fig. 1e, purple), fitted the contour to an ellipse (Extended Data Fig. 1e, dashed yellow) and used the long axis of the ellipse as the longitudinal direction (Extended Data Fig. 1e, solid yellow line). We defined the location of the anterior and posterior ends of the embryo to be the location on the embryo contour that intersected with this longitudinal axis (Extended Data Fig. 1f). We defined the transverse direction to be orthogonal to the longitudinal direction.

Analysis of spindle oscillations. Centrosome motions. To determine the amplitude and timing of centrosome oscillations, we examined the transverse position of the centrosomes, obtained rough peak positions by identifying local maximum and minima after smoothing the trajectories and then obtained refined peak positions by fitting the raw data for the unsmoothed transverse positions around these local maxima and minima to Gaussians (Extended Data Fig. 1g).

We analysed the impact of laser-ablation arc cuts (Fig. 1e–j and Extended Data Fig. 2a) on oscillations by calculating  $\Delta v_y = v_{y(after)} - v_{y(before)}$ , the difference in centrosome (y) velocity immediately before  $v_{y(before)}$  and after ablation  $v_{y(after)}$  (Extended Data Fig. 2b). Ablation itself took a time window  $\tau_w$  of 2.3 s on average to complete. Velocities were measured by linear fits of transverse centrosome positions over for a mean of 2.7 s (at least three data points, Extended Data Fig. 2c, for example). The resulting change in the centrosome transverse velocity ( $\Delta v_y = v_{y(after)} - v_{y(before)}$ ) was calculated for all arc-cut experiments shown in Fig. 1e, f, h, i ( $\Delta v_y$  in Extended Data Fig. 2d).

We analysed the impact of laser-ablation double rectangular plane cuts (Extended Data Fig. 2e) and open-cylindrical cuts (Fig. 2a–c and Extended Data Fig. 2f) on oscillations by calculating  $A_{\rm after}/A_{\rm before}$ , the ratio of amplitudes for the oscillations immediately before  $A_{\rm before}$  and after  $A_{\rm after}$  the cuts (Extended Data Fig. 2g). Both double-plane cuts and open-cylindrical cuts exhibited a highly significant difference in the  $A_{\rm after}/A_{\rm before}$  ratio compared to controls (Extended Data Fig. 2h).

We analysed the impact of laser-ablation cup cuts (Extended Data Fig. 2i) on oscillations by calculating the minimum distance  $d_{\min}$  that the centrosome came to the cell boundary after ablation (Extended Data Fig. 2j).

Analysis of astral microtubules. To measure the changes in astral MTs during spindle oscillations, we imaged GFP::B-tubulin in 11 embryos and calculated the intensity of pixels in three annular sectors with a 3 μm inner radius, a 9 μm outer radius and subtended angles of 60° (Extended Data Fig. 6a); an 'up' transverse section oriented in the direction of centrosome motion, a 'down' transverse section oriented in the direction opposite centrosome motion and a 'lateral' section between the centrosome and the lateral cortex. The orientations of the annular sectors remained unchanged while their locations varied as the posterior centrosome moved (Supplementary Video 7). For each embryo, we measured the tubulin intensity with background subtraction in these three regions throughout the five-half-cycle temporal window with the maximal five consecutive peak-to-valley amplitudes (for example, see Extended Data Fig. 6b, left panel). Two full cycles of the upward part (positive y direction,  $T_1$  and  $T_2$ ) and two full cycles of the downward part (negative y direction,  $T_3$  and  $T_4$ ) after vertical flipping were taken into consideration (Extended Data Fig. 6b, middle panel), giving a total of 44 full oscillation cycles from 11 embryos. For each full cycle, the time period was rescaled to the mean time period  $T_{(m)}$  of the 44 cycles (Extended Data Fig. 6b, right panel), and the intensity values from the transverse region were further normalized by the temporal mean intensity of the lateral region. After aligning the oscillation midpoints at zero, all amplitude values were divided by half the mean transverse displacement (maximum y value minus minimum y value) of the 44 cycles, to set the amplitude nearly between 1 and -1.

To analyse the predicted changes in astral MTs during spindle oscillations from the coarse-grained model, we derived an analytical formula for the total length of MTs in an annular sector (which is analogous to the experimentally measured intensity of tubulin in such a sector). To do this, we consider an angle  $\theta' \in [-\pi, \pi]$  encircling the centrosome in the coarse-grained model, where  $\theta'$  is related to the polar angle  $\varphi'$  (defined in Supplementary Notes Section II.v) by  $\theta' = \varphi'$  for  $\theta' > 0$  and  $\theta' = -\varphi'$  for  $\theta' < 0$ . Consider a discal sector  $S = [D_1, D_2] \times [\theta'_1, \theta'_2]$ , where we assume that  $D_{1,2} < d(\theta')$  for  $\theta'_1 \le \theta' \le \theta'_2$ . There are three types of MTs emanating from the centrosome: (1) those with length  $l \le D_1$ , which contribute nothing to the discal intensity; (2) those with length  $l \le l \le D_2$ , which contribute a length of  $l - D_1$  and (3) those with length  $l \le l \le D(\theta')$ , which contribute a length of  $l \ge D_1$ . Hence, the total MT length in  $l \le l$ 

$$\begin{split} L &= \int_{\theta_1^l}^{\theta_1^l} \mathrm{d}\theta^l \left[ \int_{D_1}^{D_2} \mathrm{d}l \left( l - D_1 \right) \psi \left( l \right) + \int_{D_2}^{D(\theta^l)} \mathrm{d}l \left( D_2 - D_1 \right) \psi \left( l \right) \right] \\ &= \int_{\theta_1^l}^{\theta_1^l} \mathrm{d}\theta^l \left[ 1 - \frac{D_2 - D_1}{l_{\text{MT}}} \frac{\exp(-D(\theta^l)/l_{\text{MT}})}{\exp(-D_1/l_{\text{MT}}) - \exp(-D_2/l_{\text{MT}})} \right] \end{split}$$

with  $l_{\rm MT}=V_{\rm g}/\lambda$  and using that  $\psi(l)=\frac{\gamma}{V_{\rm g}}\exp(-l\lambda/V_{\rm g})$ .

Simulations with the coarse-grained model of cortical pulling. We numerically calculated the centrosome movement using the equations of motion from our coarse-grained model of cortical pulling. Balancing the net force from the force generators ( $F_{\rm fg}$ ) with the drag force of the centrosome ( $F_{\rm drag}$ ) gives  $F_{\rm drag}+F_{\rm fg}=0$ , resulting in

$$\dot{Y} = \frac{Mf_0}{2\eta} \int_0^{\pi} d\varphi \sin\varphi \frac{W}{\sqrt{W^2 - 2WY \cos\varphi + Y^2}} \left(\cos\varphi - \frac{Y}{W}\right) P(\varphi)$$

And the dynamical equation for *P* can also be derived from the equations of motion:

 $\partial_t P(\varphi) = \Omega\left(\dot{Y},Y,\varphi\right)(1-P(\varphi)) - \kappa P(\varphi)$ , where the impingement rate is given by:

$$\Omega\left(\dot{Y}, Y, \varphi\right) = \left(\dot{Y}\cos\varphi + \frac{V_{\rm g}W - V_{\rm g}Y\cos\varphi}{d}\right) \frac{1}{2} \left(1 - \frac{1}{\sqrt{1 + \left(r/d\right)^2}}\right) \frac{\gamma}{V_{\rm g}} e^{-d\lambda/V_{\rm g}},$$

and  $d = \sqrt{W^2 - 2WY \cos \varphi + Y^2}$ .

Then, we can numerically calculate the centrosome velocity and position and the probability of force generators being bound using estimated motor numbers for different stages. Using a motor number slightly higher than  $M_c$ , we can produce anaphase oscillation behaviours. Using a motor number much lower than  $M_c$  while keeping all the other parameters the same, we can simulate PNC centration. Finally, we use the same motor number for PNC to simulate the spindle stable centring in the metaphase as in the experiments of Garzon-Coral et al.  $^{16}$ , where an external force ( $F_{\rm ext}$ ) was exerted and then released. Under this condition, the force-balance equation becomes:

$$F_{\rm drag} + F_{\rm fg} + F_{\rm ext} = 0$$

We swept the parameters in the simulations to investigate how the biophysical parameters affect the centrosome movements. Extended Data Fig. 5a-c gives examples of pronuclear centration, metaphase stable centring and centrosome oscillation while different parameters were swept. Extended Data Fig. 5d-h demonstrates how varying different parameters affected the outcome observations. Finally, we adopted the parameters shown in Extended Data Table 1, which yielded realistic results like those from the experiments. These simulation data are shown in the main text and figures.

**Measuring cytoplasmic fluid flows with FNDs.** We measured cytoplasmic fluid flows using FNDs as passive tracer particles. This entailed tracking the motions of individual FNDs and averaging the velocities of FNDs over multiple time points and embryos to determine the fluid flow velocities.

We imaged FNDs in embryos by 3D time-lapse microscopy with either 9 or 15 z sections spaced 1 µm apart. We adopted and modified the MATLAB 3D feature finding algorithms, which were written by Yongxiang Gao and Maria Kilfoil<sup>70</sup> based on IDL codes from John C. Crocker and David G. Grier<sup>69</sup>, to extract the FND particle features and obtain their 3D positions with subpixel precision. Then we tracked the 3D trajectory of each individual FND again using the MATLAB Particle Tracking Code Repository. We calculated the 3D instantaneous velocity of every FND, at each time and location, as the difference between its positions at two consecutive frames divided by the time interval between those frames. While tracking FNDs, we also imaged and tracked centrosomes using GFP::\(\textit{B}\)-tubulin images.

To determine the pattern of fluid flow throughout the cytoplasm. we averaged together FND velocities from different time points and embryos. Positioning stages can mainly be recognized through GFP::β-tubulin images. We also used the position and movement of the centrosomes to determine the frames to include and the coordinate system with which to perform this averaging. For spindle oscillations midpoints at time  $T_{\rm m}$ , we selected times in which the posterior centrosome was located within 1 µm transversely from the oscillation midpoint and moving with a transverse speed greater than  $0.15 \, \mu m \, s^{-1}$ . For prometaphase spindles, we included times after rotation had nearly ceased. For metaphase spindles, we included spindles with lengths between 20% and 40% of their embryo lengths and before spindle oscillations had begun. After determining which time points to include, we aligned the position and velocity data based on the locations of the centrosomes and the embryos' anterior-to-posterior directions. Then we projected the 3D positions and instantaneous velocity vectors of the FNDs onto the x-y plane and determined the 2D fluid flow velocity on grid points with 2.5  $\mu$ m (x) by 2.5  $\mu$ m (y) spacing (Extended Data Fig. 3a) by averaging FND velocities in overlapping cuboid domains. From the prometaphase to the late anaphase (Figs. 3e and 4g,j), the averaging domain was a 5  $\mu$ m (x) by 5  $\mu$ m (y) by 6  $\mu$ m (z) cuboid with the grid point at the cuboid centre (Extended Data Fig. 3b). To calculate fluid flows around pronuclei (Fig. 5e), we used a 5  $\mu$ m (x) by 5  $\mu$ m (y) by 9  $\mu$ m (z) overlapping averaging domain (Extended Data Fig. 3c). For PNC migration and rotation, we considered two different criteria for averaging: (1) As in the main text (Fig. 5e), we adopted times when the longitudinal distance between the PNC centre and the embryo posterior end measured 35-50% of the embryo length (or R=0.35-0.5; Extended Data Fig. 3g, left). (2) Alternatively, we used times when the angle A between the PNC axis (centrosome-to-centrosome) and the longitudinal axis of the cell ranged between  $33^\circ$  and  $66^\circ$  (Extended Data Fig. 3d, right). Both methods gave qualitatively similar results.

The averaged experimental velocity vectors were plotted according to a *P*-value-related colour map. The *P* value of each cuboid block of 2D velocity data was calculated with a one-sample two-tailed *t*-test using the lengths of those pooled velocity vectors projected onto the direction of their averaged vector. The null hypothesis is that there is no cytoplasmic flow and particles merely exhibit Brownian motion. The colour map makes those significant flow vectors more prominent to improve visibility. Finally, we drew an imaginary embryo cell contour to represent the averaged cell boundary and removed those data points outside the drawn boundary.

To compare the computational fluid mechanics simulations to the experimental data, we performed analogous projections and averaging. For the simulations, we calculated projected 2D vector fields of fluid flow on 2  $\mu m$  by 2  $\mu m$  grids by averaging the continuous velocity field in overlapping domains. For simulations from the prometaphase to the late anaphase (Figs. 3b,c, 4e,f and 4h,i), we used a 4  $\mu m$  (x) by 4  $\mu m$  (y) by 6  $\mu m$  (z) cuboid averaging domain. For simulations at the PNC stage (Fig. 5c,d), we used a 4  $\mu m$  (x) by 4  $\mu m$  (y) by 8  $\mu m$  (z) cuboid averaging domain.

#### Data availability

All data in this study are available from the corresponding authors upon reasonable request.

#### **Code availability**

The codes used in this study are available from the corresponding authors upon reasonable request.

#### References

- Walston, T. & Hardin, J. An agar mount for observation of Caenorhabditis elegans embryos. Cold Spring Harb. Protoc. https://doi.org/10.1101/pdb.prot5540 (2010).
- Crocker, J. C. & Grier, D. G. Methods of digital video microscopy for colloidal studies. J. Colloid Interface Sci. 179, 298–310 (1996).
- Gao, Y. & Kilfoi, M. L. Accurate detection and complete tracking of large populations of features in three dimensions. Opt. Express 17, 4685–4704 (2009).

#### **Acknowledgements**

Worm strains were provided by M. Delattre and the Caenorhabditis Genetics Center. M.J.S. acknowledges support from the National Science Foundation (NSF) under awards DMR-1420073 (NYU MRSEC) and DMR-2004469. D.J.N. acknowledges NSF grant DBI-1919834, NSF grant 2004380, and the National Institutes of Health grant 1R01GM104976-01. We are grateful to C.-H. Yu who assisted with the optical setup and to C.-Y. Fang for advice on FND surface treatment. We also like to thank R. Farhadifar for helpful discussion over the whole project and advice on modelling, Y.-N. Young for assistance in a technical calculation and J. Howard for helpful discussions.

#### **Author contributions**

H.W., D.J.N. and M.J.S. designed the research. H.W. developed the FESLA setup. H.W. conducted all the experiments and data analysis. H.C. provided support for the FND experiments. G.K., E.N. and M.J.S. worked on the large-scale fluid mechanics simulations. M.J.S. and D.J.N. derived and analysed the coarse-grained model. H.W., D.J.N., M.J.S., E.N. and G.K. wrote the paper.

#### **Competing interests**

The authors declare no competing interests.

#### **Additional information**

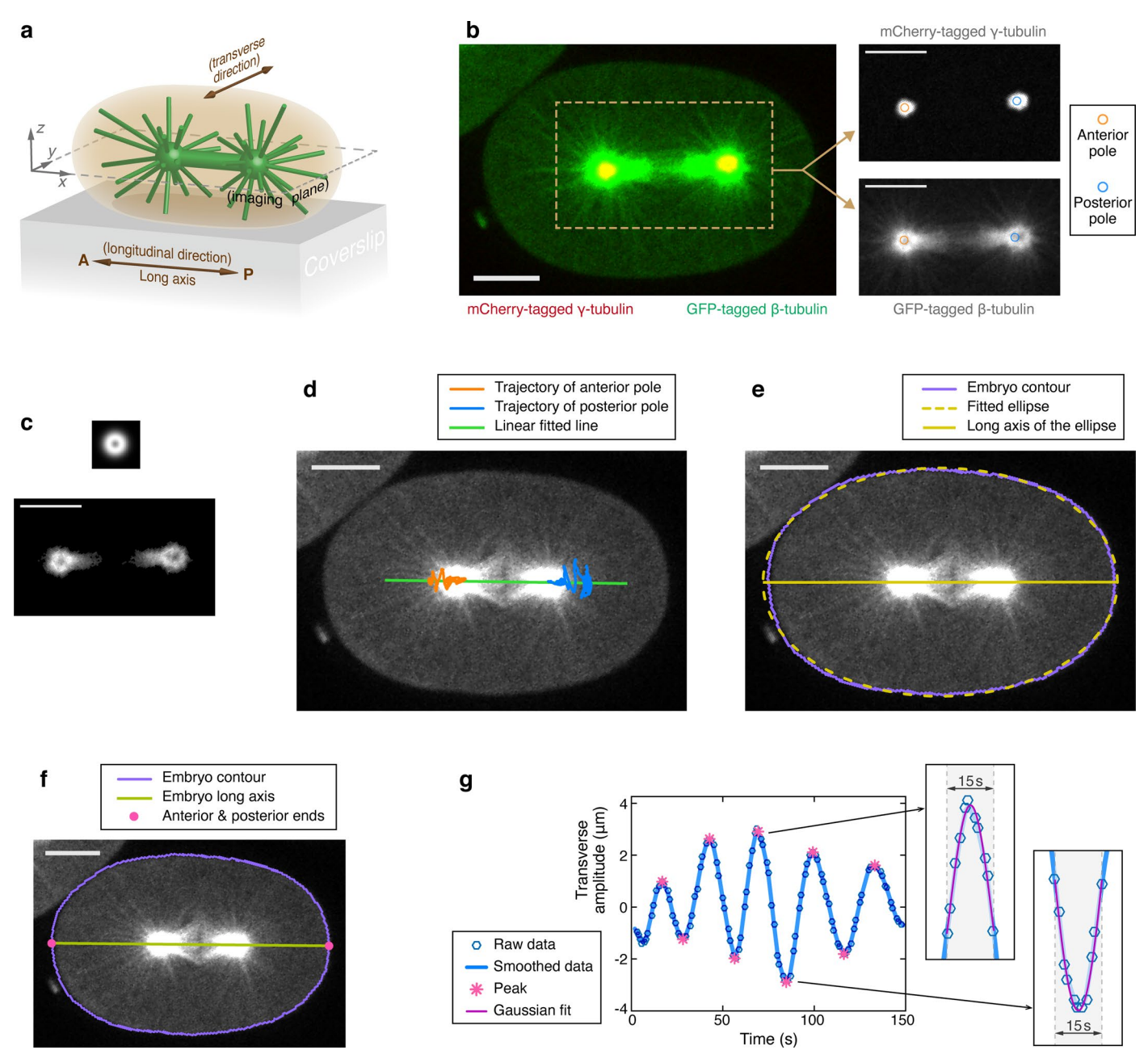
**Extended data** Extended data are available for this paper at https://doi.org/10.1038/s41567-023-02223-z.

**Supplementary information** The online version contains supplementary material available at https://doi.org/10.1038/s41567-023-02223-z.

 $\begin{tabular}{ll} \textbf{Correspondence and requests for materials} should be addressed to Hai-Yin Wu. \end{tabular}$ 

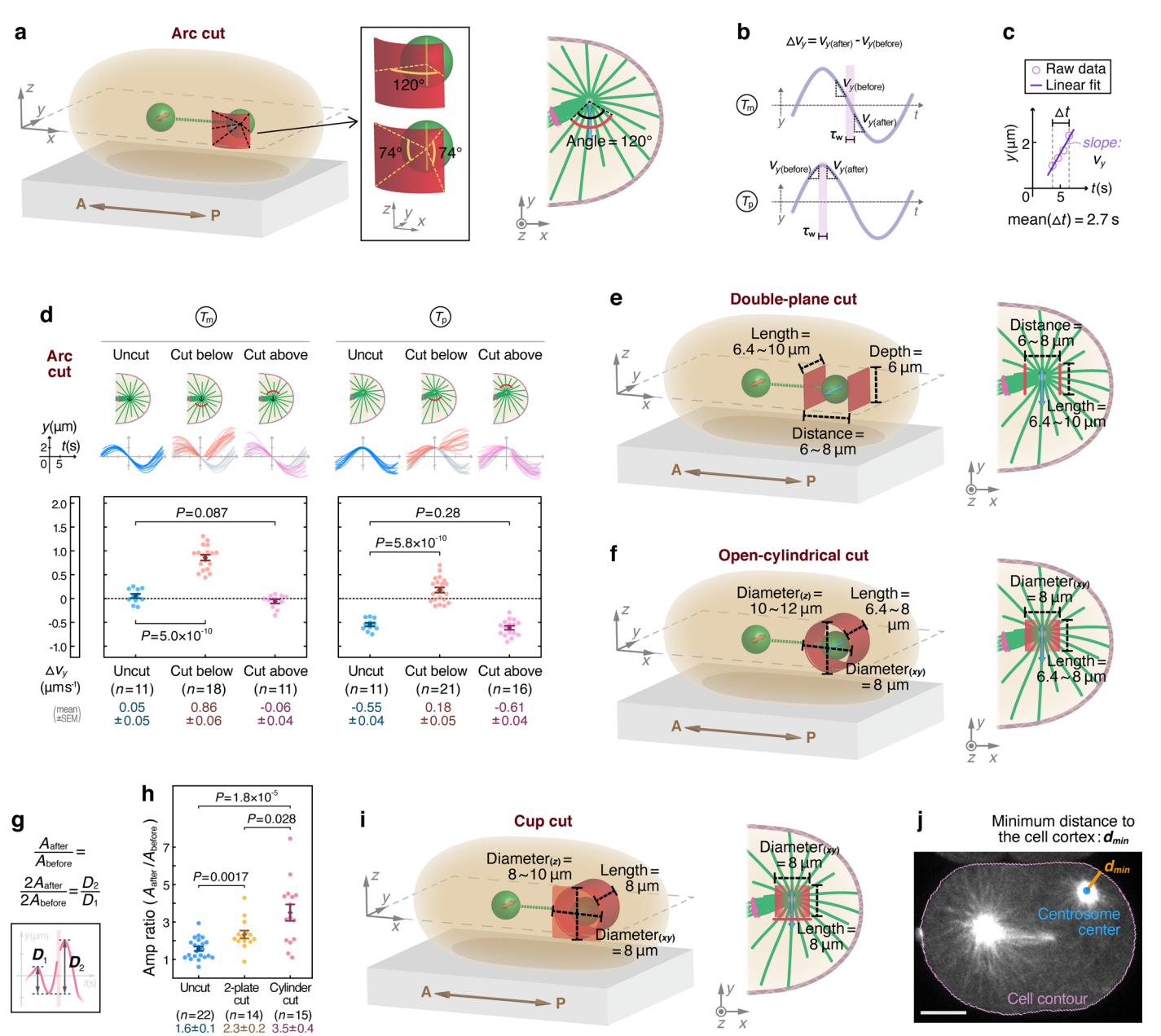
**Peer review information** *Nature Physics* thanks Jan Brugues and the other, anonymous, reviewer(s) for their contribution to the peer review of this work.

**Reprints and permissions information** is available at www.nature.com/reprints.



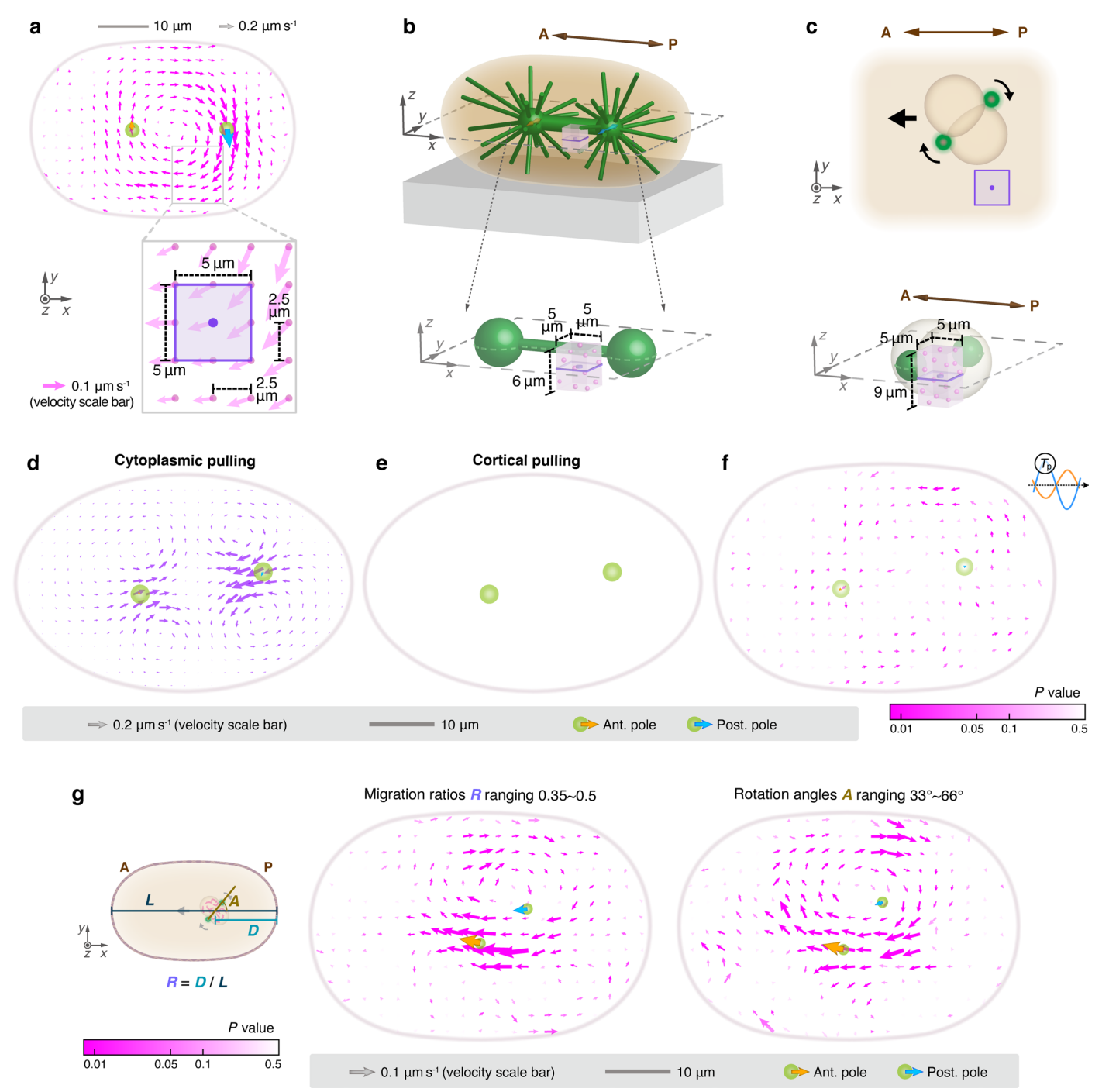
Extended Data Fig. 1 | Orientation terminology, image analysis and centrosome motion quantification. a, The configuration and the terminology of embryo orientation used in this study. The mitotic spindle is simply illustrated by the green dumbbell, while astral MTs illustrated by slender green sticks. The confocal imaging plane, which is parallel to the coverslip, is defined as the x-y plane, with the z = 0 plane falling at the centre of the spindle or the PNC. The embryo's A-P direction is assigned as the longitudinal direction (x axis), with the embryo's posterior end facing the positive x direction. And the transverse direction refers to the y direction. **b**,**c**, An example of the centrosome-tracking image. **b**, The two-colour merged image of an *C. elegans* embryo expressing mCherry-tagged γ-tubulin (red) and GFP-tagged β-tubulin (green). The two separate images of the dashed-line region are shown in the right panel. The upper one is a γ-tubulin-labeling image with its labeled centrosome locations derived by MATLAB Particle Tracking Code Repository by Daniel Blair and Eric Dufresne. The lower one is a β-tubulin-labeling image, while its centrosome information is derived from the particle tracking code plus the second-step

correlation method.  $\mathbf{c}$ , Top, the square image patch with the artificial ring structure mimicking a centrosome. Bottom, an example of the post-processed (background-subtraction and thresholding) β-tubulin-labeling image used for correlation calculation. (The top and bottom images are displayed on the same scale.)  $\mathbf{d}$ ,  $\mathbf{e}$ , The information of the embryo long axis (or longitudinal direction) can be extracted automatically in two ways: d, through linear fitting on the trajectory data of the anterior and posterior centrosomes, or e, through fitting the automatic detected embryo contour with a simple ellipse. f, An example of the automatic detected embryo contour and the embryo anterior/posterior ends. g, An example of oscillation peak detection. The crests/troughs (or the peak points) of the transverse oscillations were calculated by (1) first finding the local maxima/minima from the smoothed amplitude data, and then (2) fitting the raw amplitude data, which fall within the 15-second windows around the above detected maxima/minima, by Gaussian function (see the enlargements). The derived peak points are marked by pink asterisks. All scale bars on images are 10 μm.



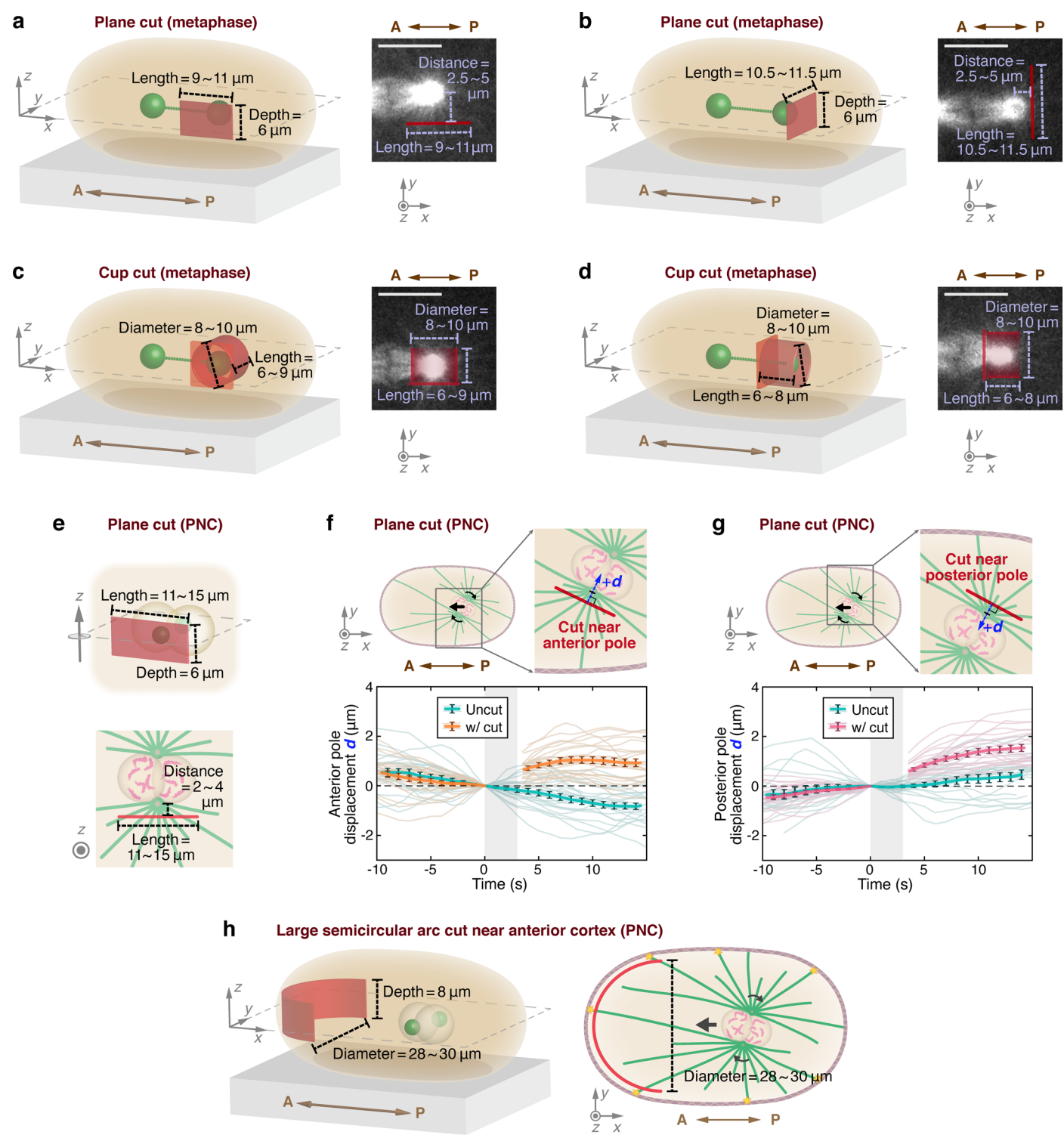
Extended Data Fig. 2 | Dimensions of laser ablations performed during transverse spindle oscillations and the results quantifications. In 3D schematics a, e, f, and i, centrosomes are represented by two green balls and the spindle body is simplified into the green dashed line. The A-P direction (embryo polarity) is indicated by the brown arrow. The orange and blue arrows displayed on the centrosomes imply the transverse oscillations of the anterior and posterior centrosomes respectively. The posterior part of the corresponding x-y imaging midplane (2D view from the top) is exhibited on the right of each 3D schematic, with the spindle and astral MTs sketched in green and chromosomes in magenta. All ablation geometrics are portrayed in red for both 2D and 3D schematics. a, Dimensions of the arc cuts in Fig. 1e,f, and h,i (all performed with the same angular span stated here). b,c, Calculation of centrosome velocity change  $(\Delta v_y)$  for arc cuts. **b**, Definition of  $\Delta v_y$  at timing  $T_m$  and  $T_p$  respectively. And  $\tau_{w}$  is the sandwiched window (for ablated embryos: this window is the ablation execution time) between the two intervals  $\Delta t$  used for calculating centrosome transverse velocity  $v_{v(loefore)}$  and  $v_{v(after)}$ . **c**, The raw data of centrosome position falling within the interval  $\Delta t$  are used to calculate transverse (y) velocity by linear fitting. **d**, The  $\Delta v_y$  data for uncut (control) and arc-cut embryos. Left, the data

for Fig. 1e,  $f(T_m)$ . Right, the data for Fig. 1h,  $i(T_n)$ . e, A schematic of the double rectangular (y-z) plane cut and the detailed dimensions. **f**, Dimensions of the open-cylindrical cuts in Fig. 2a-e. g, Measurement on oscillation amplitude change by calculating the amplitude ratio  $A_{after}/A_{before}$  (mentioned in Fig. 2e). The notation A means oscillation transverse amplitude, and D stands for peakto-valley transverse amplitude/displacement. The oscillation example (pink curve) is the one from Fig. 2d (open-cylindrical cut). The ablation execution is highlighted by the light pink vertical strip. h, The comparison of the amplitude ratios among uncut, double-plane-cut, and open-cylindrical-cut embryos. We found that the more perpendicular MTs that were ablated, the more the oscillation amplitude increased. This is consistent with the perpendicular MTs being subject to pulling forces, and hence constraining centrosome motion.  ${f i}$ , Dimensions of the cup cuts in Fig. 2f-i.  ${f j}$ , An example image of calculating the minimum distance to the cell cortex (mentioned in Fig. 2i). The minimum distance, from the posterior centrosome to the cell cortex, of each embryo, is extracted from the time frame with minimal  $d_{min}$  (scale bar, 10  $\mu$ m). All P values were calculated by two-tailed Student's t-tests (error bars, SEM).



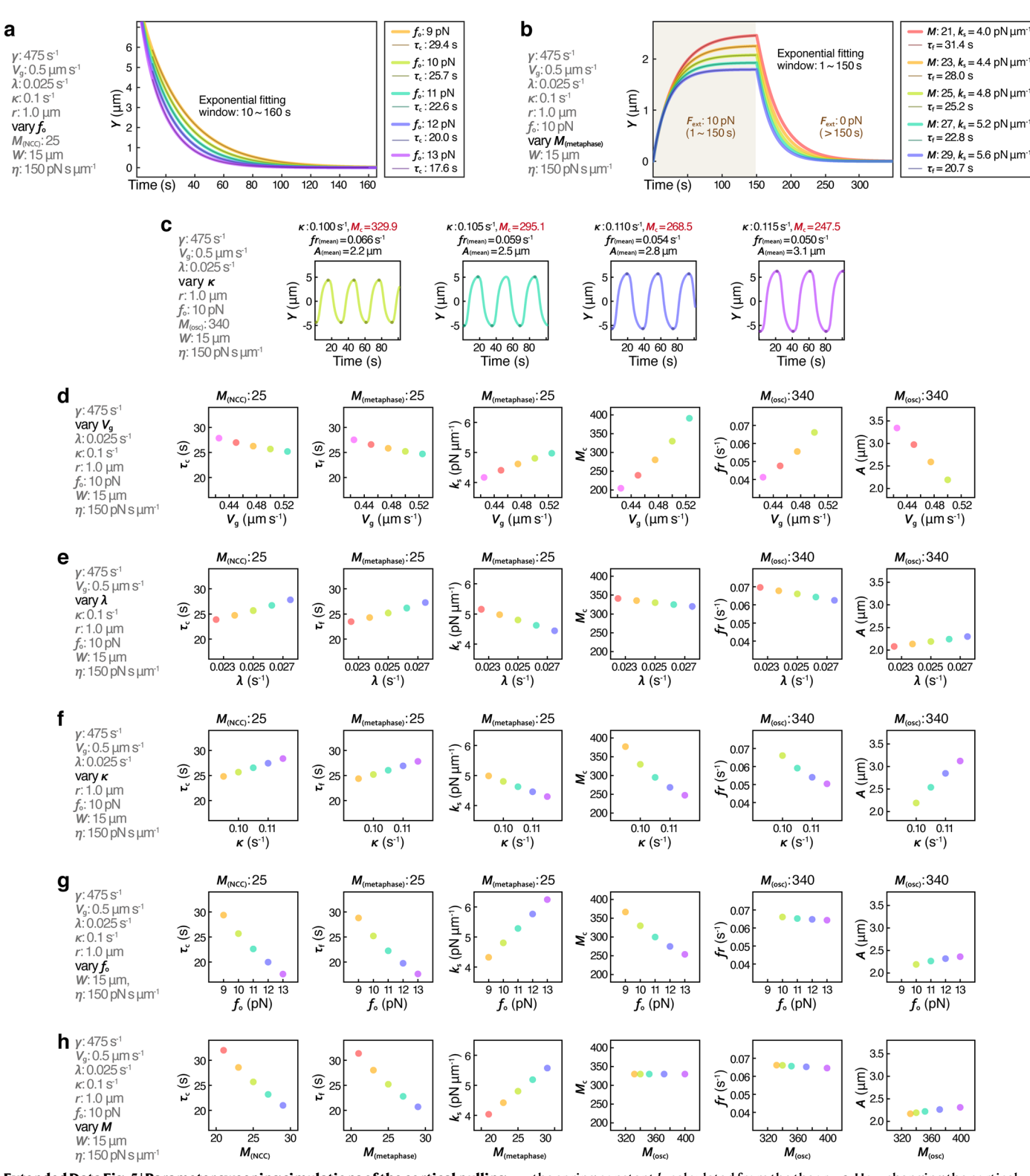
Extended Data Fig. 3 | Averaging operations for experimental flow measurements and fluid results. a, The fluid flow vector field is displayed by 2D vectors (magenta arrows) plotted on grid points with 2.5  $\mu$ m x spacing and 2.5  $\mu$ m y spacing (the bottom enlargement). After proper alignment and data grouping, each velocity vector represents the mean x-y velocity of the FNDs located within the averaging domain surrounding the centre grid point (the purple square frame surrounding the purple dot, further described in b and c). b,c, Schematics of the averaging cuboid domain (purple transparent cuboid) with the grid point located at the centre of the cuboid. Centrosomes are illustrated by green balls, and the magenta particles inside the cuboids represent tracked FNDs. The A–P direction is indicated by the brown arrow. b, For prometaphase to late anaphase, the averaging domain is a 5  $\mu$ m (x) by 5  $\mu$ m (y) by 6  $\mu$ m (z) cuboid. Spindles are aligned onto the x-y midplane (z = 0), at which plane the mean 2D projection vector field is plotted. And the purple frame

(3D view) is the purple square frame in **a. c**, An exception for the PNC stage, the averaging cuboid measures  $5 \, \mu m$  (x) by  $5 \, \mu m$  (y) by  $9 \, \mu m$  (z) (larger size in the z direction). The purple square in the upper panel is the purple frame (3D view) in the bottom panel. **d**, **e**, The simulated fluid flows (in the x-y plane of spindle motion) at the peak of the oscillations, time  $T_p$ , under (**d**) the cytoplasmic pulling or (**e**) the cortical pulling models. **f**, The experimental flow vector field derived from averaging the movements of tracked FNDs in 17 embryos at time  $T_p$ . **g**, Left, definition of pronuclear migration/centration and rotation progression. Middle, the averaged pronuclear experimental fluid data with migration ratio  $R = 0.35 \cdot 0.5$  (the same data as Fig. 5e). Right, the data with rotation angle  $A = 33^{\circ} \cdot 66^{\circ}$ . For all experimental fluid data, the statistical significance of the velocity vectors is indicated by their colour scale (*P*-value colour bar) (see Methods for details). Arrows on centrosomes indicate mean measured centrosome velocities.



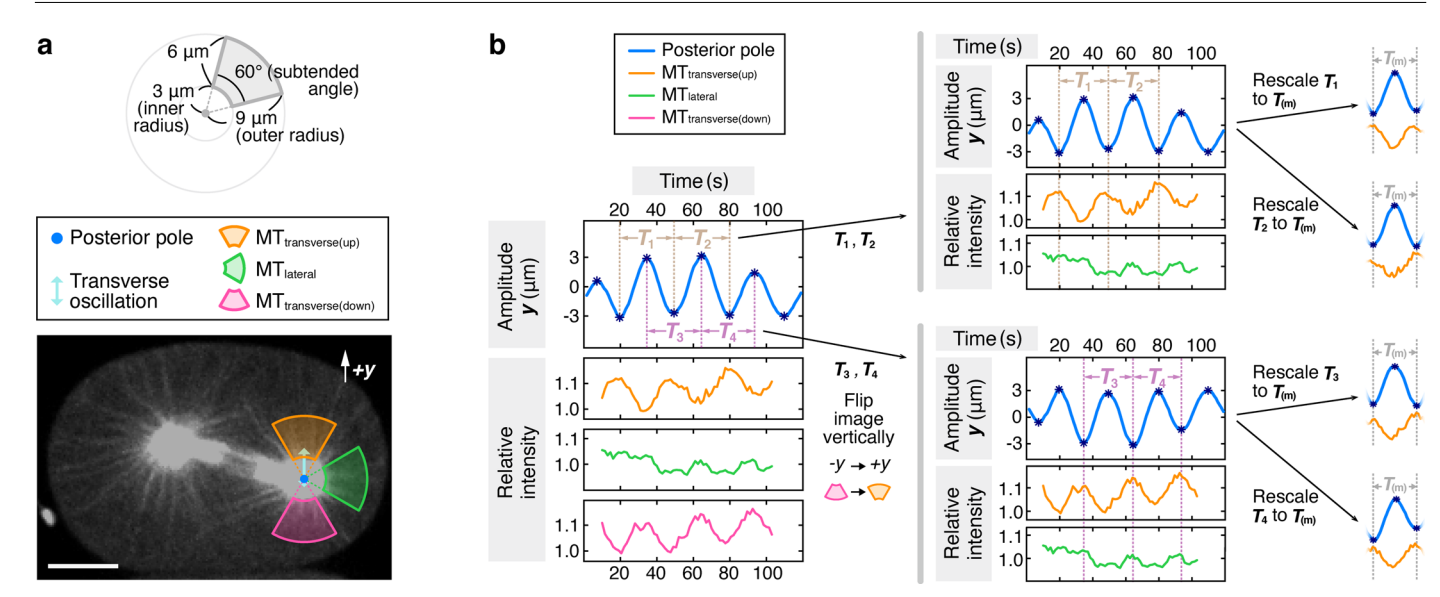
**Extended Data Fig. 4** | **Dimensions of laser ablation experiments performed in metaphase and the PNC stage.** Centrosomes are presented by green balls in all 3D schematics. Centrosomes and astral MTs are sketched in green and chromosomes in magenta in all 2D schematics. All ablation geometrics are portrayed in red. The A-P directions are indicated by brown arrows. **a,b**, Metaphase: dimensions of the rectangular plane cuts in Fig. 4a,b respectively. **c,d**, Metaphase: dimensions of the cup cuts in Fig. 4c,d respectively. **e**, The PNC stage: dimensions of the rectangular plane cuts in Fig. 5a,b. **f,g**, The PNC stage: the plane cuts near the anterior or leading centrosomes (**f**), and the plane cuts near the posterior or trailing centrosomes (**g**). Both upper parts are the schematics showing the definition of centrosome centre displacement *d*,

which is the relative orthogonal (away from the plane cut) displacement from the locus right before cutting. The black arrows indicate the progression of pronuclear migration and rotation. The mean displacement results with SEM error bars, including uncut and cut embryos, are shown in both lower parts. Their raw data are plotted semi-transparently in the back layer. Sample numbers are  ${\bf f}$ , n=25 (uncut), n=25 (with cut) and  ${\bf g}$ , n=23 (uncut), n=23 (with cut). And the data in Fig. 5b is the combination of these two data sets ( ${\bf f}$  and  ${\bf g}$ ), including both plane cuts near the leading and the trailing centrosomes.  ${\bf h}$ , The PNC stage: dimensions of the large semicircular arc cuts (near anterior cortices) in Fig. 5f–h. All scale bars on images are 10  $\mu$ m.



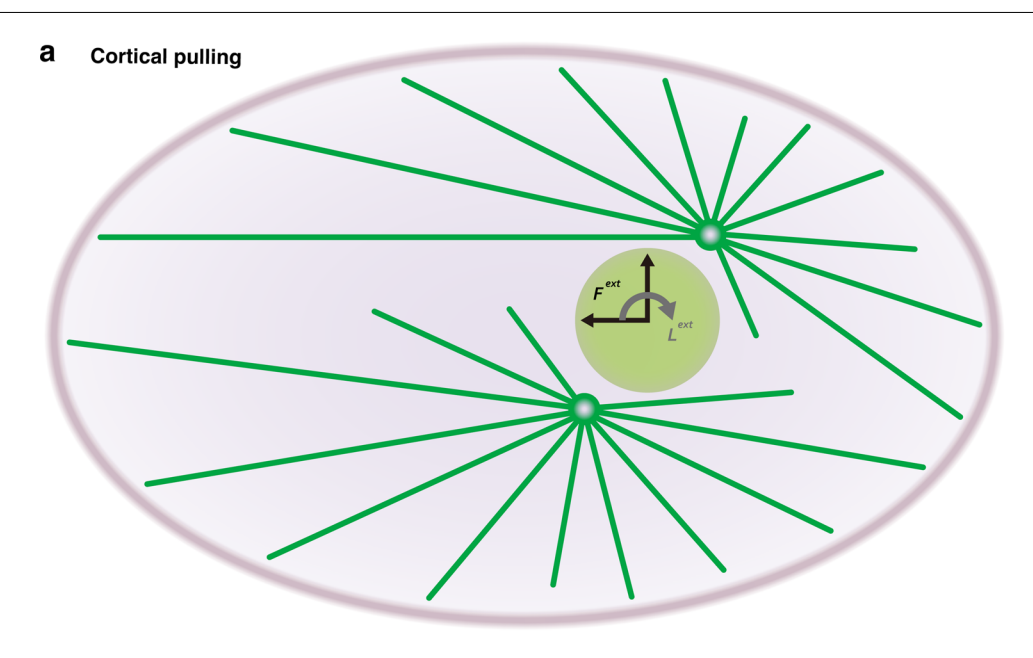
**Extended Data Fig. 5**| **Parameter sweeping simulations of the cortical pulling model. a-c**, The examples of simulated centrosome movements while parameter sweeping. **a**, How varying the pulling force  $f_0$  per force generator affects the PNC centration and the corresponding exponential fitting of  $\tau_c$ . **b**, How varying the motor number M in metaphase affects the stable centring behavior under the condition of exerting an external force for 150 seconds and releasing. The centrosome motion is shown with the corresponding exponential fitting of  $\tau_t$  and

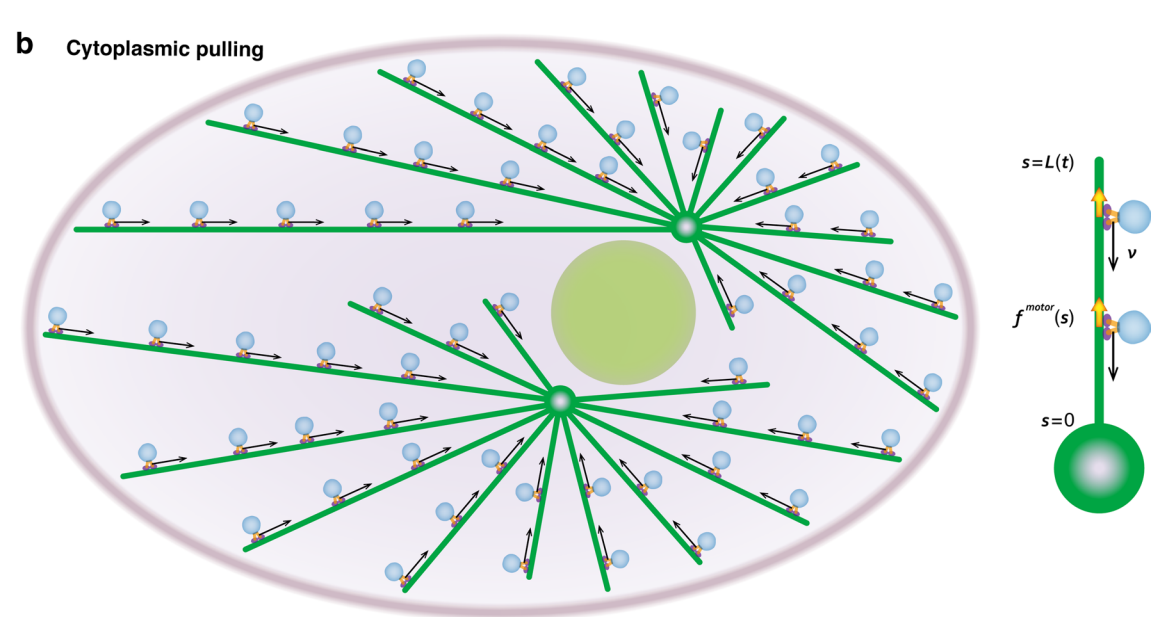
the spring constant  $k_s$  calculated from the theory.  $\mathbf{c}$ , How changing the cortical motor detachment rate  $\kappa$  affects the spindle oscillations. The corresponding  $M_c$  were derived from the theory and we adopted the same motor number (above all  $M_c$ ) to simulate the oscillations. The averaged oscillation frequencies and amplitudes are specified.  $\mathbf{d}$ - $\mathbf{h}$ , The results of PNC centration ( $\tau_c$ ), metaphase stable centring ( $\tau_f$  and spring constant  $k_s$ ), and anaphase oscillation ( $M_c$ , and oscillation frequency and amplitude) under different parameters.



Extended Data Fig. 6 | Quantification of astral MTs intensity during transverse oscillations. a, One snapshot from the example GFP:: $\beta$ -tubulin time-series with the assigned transverse and lateral annular-sector regions shown

(scale bar, 10  $\mu$ m). The dimensions of the annular sectors are depicted on the top. **b**, Detailed information about data alignment for intensity measurement. Please refer to Methods for detailed operations.





#### C

#### Initial (x,y) position values $(\mu m)$

Object \ Event	oscillation (T <sub>m</sub> )	oscillation ( $T_p$ )	prometaphase	metaphase elongation	pronuclear migration
posterior centrosome	(12.7, 0)	(12.2, 1.7)	(6.2, 0.5)	(8.9, 0)	(7.3, 2.6)
spindle/pronuclei(PNC)	(3.3, -0.05)	(2.75, 0)	(0.8, 0)	(1.65, 0)	(3.7, 0)
anterior centrosome	(-6.1, -0.1)	(-6.7, -1.7)	(-4.6, -0.5)	(-5.6, 0)	(0.1, -2.6)

### $\label{lem:prop:prop:models} Extended \ Data \ Fig. \ 7 \ | \ Models \ of the force transduction mechanisms \ and initial position values in computational fluid dynamics simulations.$

**a,b**, Schematics for the computational models of the force transduction mechanisms. The figure shows the PNC stage (see Fig. 5e for the corresponding experiment). Our simulations have five structural elements: the cell cortex (gray purple ellipses), the spindle/pronuclei (light green circles), the centrosomes (green circles), elastic MTs (green lines) and the cytoplasm, the fluid filling inside the cortex. **a**, Cortical pulling. Due to the cortical pulling forces, MTs remain straight and the forces directly act on the PNC without any loss for the MT bending. Hence, in a short time horizon, the cytoplasmic flow arises from the

translation and rotation of the pronuclei-centrosome- MT complex. We model that mechanism by applying an external force  $\mathbf{F}^{\rm ext}$  and torque  $\mathbf{L}^{\rm ext}$  on the PNC.  $\mathbf{b}$ , *Cytoplasmic pulling*. Cytoplasmic dynein motors attach to the MTs and walk towards the centrosomes with velocity  $\mathbf{v}$  (black arrow). As they do so, they apply a pulling force on the MTs in the opposite direction to their motion. We model the force applied by the motors by a continuum model:  $\mathbf{f}^{notor}(s)$ .  $\mathbf{c}$ , The initial (x,y) positions (in  $\mu$ m) of the spindle's (or pronuclei's) and the centrosomes' centres in the simulations. All objects are at z=0. We decided on those values based on the experiments (see Fig. 3e for oscillation, Fig. 4g for prometaphase, Fig. 4j for metaphase elongation, and Fig. 5e for the pronuclear migration).

#### Extended Data Table 1 | Simulation parameters for the cortical pulling coarse-grained model

Simulation parameter	Value	References	
spherical cell radius	15 [μm]	Estimated in this study.	
microtubule growth rate $(V_g)$	0.5 [μm s <sup>-1</sup> ]	71	
microtubule catastrophe rate $(\lambda)$	0.025 [s <sup>-1</sup> ]	46	
microtubule nucleation rate $(\gamma)$	475 [s <sup>-1</sup> ]	72	
microtubule-force-generator detachment rate $(\kappa)$	0.1 [s <sup>-1</sup> ]	53	
force-generator capture radius $(r)$	1.0 [μm]	46, 51	
force-generator pulling force $(f_0)$	10 [pN]	46	
centrosome drag $(\eta)$	150 [pN s μm <sup>-1</sup> ]	16	